ARL-TR-9388 ● JAN 2022

DEVCOM ARMY RESEARCH LABORATORY

Performance Analysis of Side-Looking Ground Penetrating Radar Imaging

by Traian Dogaru

NOTICES

Disclaimers

ARL-TR-9388 ● JAN 2022

Performance Analysis of Side-Looking Ground Penetrating Radar Imaging

Traian Dogaru
Sensors and Electron Devices Directorate, DEVCOM Army Research Laboratory

REPORT DOCUMENTATION PAGE

Form Approved
OMB No. 0704-0188

1. REPORT DATE *(DD-MM-YYYY)* January 2022	**2. REPORT TYPE** Technical Report	**3. DATES COVERED (From - To)** July–November 2021

4. TITLE AND SUBTITLE
Performance Analysis of Side-Looking Ground Penetrating Radar Imaging

5a. CONTRACT NUMBER

5b. GRANT NUMBER

5c. PROGRAM ELEMENT NUMBER

6. AUTHOR(S)
Traian Dogaru

5d. PROJECT NUMBER

5e. TASK NUMBER

5f. WORK UNIT NUMBER

7. PERFORMING ORGANIZATION NAME(S) AND ADDRESS(ES)
DEVCOM Army Research Laboratory
ATTN: FCDD-RLS-ES
Adelphi, MD 20783-1138

8. PERFORMING ORGANIZATION REPORT NUMBER
ARL-TR-9388

9. SPONSORING/MONITORING AGENCY NAME(S) AND ADDRESS(ES)
Department of Defense High Performance Computing Modernization Program
10501 Furnace Road, Suite 101
Lorton, VA 22079

10. SPONSOR/MONITOR'S ACRONYM(S)
DOD HPCMP

11. SPONSOR/MONITOR'S REPORT NUMBER(S)

12. DISTRIBUTION/AVAILABILITY STATEMENT
Approved for public release: distribution unlimited.

13. SUPPLEMENTARY NOTES
ORCID ID: Traian Dogaru, 0000-0002-1091-4928

14. ABSTRACT

This report investigates the expected performance of a side-looking ground penetrating radar (GPR) imaging systems in the presence of clutter. The analysis is based on numeric simulations of point target and clutter responses in various synthetic aperture radar configurations, capable of producing 2-D images of the underground space. Both rough surface and inhomogeneous ground are considered in the clutter models, with strong emphasis on out-of-plane imaging effects. These include image defocusing when the target location is outside the image plane. The results are presented in terms of the target-to-clutter ratio as a function of various system parameters, such as angle of incidence, range, and target burial depth. Comparisons with down-looking GPR imaging systems indicate that side-looking systems may be effective in detecting shallow buried targets, but their performance degrades rapidly in the presence of deep-buried targets.

15. SUBJECT TERMS
radar clutter, ground penetrating radar, radar imaging, radar modeling, synthetic aperture radar

16. SECURITY CLASSIFICATION OF:			**17. LIMITATION OF ABSTRACT**	**18. NUMBER OF PAGES**	**19a. NAME OF RESPONSIBLE PERSON** Traian Dogaru
a. REPORT Unclassified	**b. ABSTRACT** Unclassified	**c. THIS PAGE** Unclassified	UU	67	**19b. TELEPHONE NUMBER (Include area code)** (301) 394-1482

Standard Form 298 (Rev. 8/98)
Prescribed by ANSI Std. Z39.18

Contents

List of Figures

Acknowledgments

This work was funded by the DOD High Performance Computing Modernization Program under the Institute for Imaging Sensor Exploitation.

1. Introduction

The Signal Processing and Modeling Branch at the US Army Combat Capabilities Development Command Army Research Laboratory is currently developing unmanned aerial vehicle (UAV)-based radar imaging technology for counter-explosive hazard (CEH) applications. The explosive hazards under consideration include landmines, improvised explosive devices (IEDs), and other close-to-ground-surface targets, which have long posed major detection challenges to any kind of sensors. Since many of these targets are buried underground, ground penetrating radar (GPR) imaging has emerged as one of the technologies holding great promise to solve this problem.

This investigation continues a sequence of technical reports published by DEVCOM Army Research Laboratory[1–4] where we presented a detailed analysis of UAV-based GPR imaging systems in various configurations. The most recent of these reports examined target and clutter signatures, as well as the target-to-clutter ratio (TCR) performance metric in down-looking GPR geometries.[4] Although this is the most commonly encountered configuration in GPR applications, we are also interested in considering the side-looking sensing geometry, which is the dominant mode of operation for most synthetic aperture radar (SAR) systems.[5]

A typical side-looking, airborne SAR system forms 2-D images of the scene under interrogation in the ground plane. Such systems have been tested for CEH applications, including buried targets, with mixed success. Both computer models and experimental results have demonstrated the difficulty of detecting buried targets in airborne SAR imagery, especially when these targets are made of materials with low dielectric contrast with respect to the ground.[6,7] Some investigators have advanced the hypothesis that many positive detections in these images are due to the radar response of the disturbed soil at the burial site, rather than the targets themselves.[8–10] This response may display statistical differences from the ambient environment and show up as a contrasting feature in the SAR image. While this detection mechanism proves that airborne side-looking SAR systems can be effective in certain CEH scenarios, it is important to have a good general understanding of the radar scattering phenomenology, with the purpose of 1) operating the radar system in the optimal possible configuration and 2) reaching a correct interpretation of the imaging results.

In this work, we demonstrate that creating the SAR images in the ground plane is suboptimal in the case of buried objects due to the fact that targets placed outside the 2-D image plane appear defocused and at the wrong location. This effect is specific to underground images obtained in a dielectric medium and differs from free-space imaging scenarios. We also investigate the set of operational parameters of a UAV-based, side-looking SAR system that offers the best TCR performance. For this purpose, we undertake a study of the distributed clutter relevant to GPR applications. The major two sources of this clutter are the rough air–ground interface and the permittivity fluctuations in the soil medium. Although these two have already been investigated in our previous work in the context of down-looking GPR systems,[4] the current report emphasizes their characterization in the side-looking imaging mode.

One question we try to answer is whether horizontal or vertical plane imaging is more effective in side-looking GPR sensing. Another issue is comparing the performance of horizontal-horizontal (H-H) and vertical-vertical (V-V) polarizations for the radar antennas; both these modes have been used in the past in the side-looking SAR for CEH application and the resulting comparison has been rather inconsistent.[7,10] Other operational parameters we investigate are related to the sensing geometry and include the incidence angle, the radar platform's height and ground range, and the target burial depth. Finally, we compare the side-looking SAR configuration with the down-looking counterpart to determine the regimes they should be deployed for maximum effectiveness.

This report is organized as follows. In Section 2, we describe the side-looking GPR imaging system configurations investigated in this report and perform the point spread function (PSF) analysis of these systems. A large emphasis is placed on the out-of-plane imaging issue, which has crucial implications on the target and clutter images, as well as on the overall system performance (mathematical details related to the ambiguity curves and surfaces are developed in the Appendix). Section 3 is dedicated to characterizing the rough surface clutter in side-looking GPR imaging systems and obtaining the TCR performance figures for various sensing geometries of these systems. In Section 4 we present a limited analysis of the clutter introduced by soil permittivity fluctuations in the same context. The conclusions in Section 5 combine the results of this investigation with those derived from our previous work in the same area.

2. Description and Phenomenology of the Side-Looking GPR Imaging System

2.1 System Configuration and Simulation Methods

A schematic description of a side-looking GPR imaging system is shown in Fig. 1. This radar sensor is provided with a single transmitter (Tx) – receiver (Rx) pair, operates in monostatic configuration, and moves along a linear synthetic aperture track in the x direction. Such a system is capable of producing 2-D images, in either horizontal (x-y) or vertical (x-z) planes. In previous work we demonstrated that achieving resolution in all three directions, which would be required by a 3-D GPR imaging system, is extremely difficult with side-looking geometries.[2] Consequently, we focus this study exclusively on 2-D imaging systems.

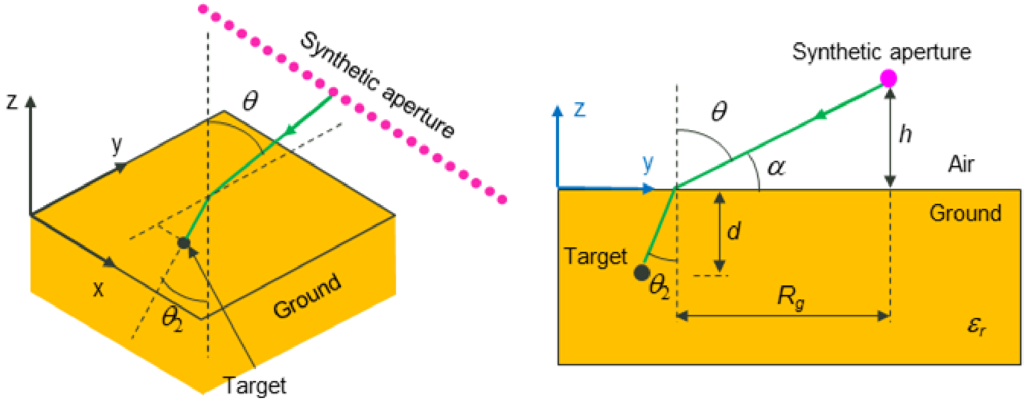

Fig. 1 Schematic representation of a 2-D side-looking GPR imaging system using a linear synthetic aperture

An important aspect of our analysis is comparing the performance of side-looking and down-looking GPR imaging systems. The latter were investigated in detail in a previous report.[4] In the current work, this comparison always refers to the 2-D versions of these imaging systems. As previously demonstrated, a 3-D down-looking GPR imaging sensor can achieve vastly superior performance when measured up against its 2-D counterpart; however, the 3-D capability for such systems in side-looking geometry is not currently available and therefore not considered in this report. The major difference between the down- and side-looking imaging configurations is that in the former case the vertical image plane is always placed directly below the synthetic aperture, whereas in the latter the image plane (vertical or horizontal) is placed at a horizontal offset range R_g in the y direction with respect to the aperture.

With a side-looking GPR system, underground images can be created in either horizontal or vertical image planes (Fig. 2). Interestingly, the downrange direction has different definitions between the two cases. Strictly speaking, the downrange direction is defined in the slant plane, along the line-of-sight (LOS). (Note: in the GPR case, the slant plane goes through the target location and makes the angle θ_2 dictated by Snell's law with the vertical axis, as shown in Fig. 3a.) However, the radar images are always created in one of the principal Cartesian planes, such as x-y (horizontal) or x-z (vertical). For images in these planes, the downrange is redefined as going along the y direction (for the horizontal plane, as in Fig. 3b) or along the z direction (for the vertical plane, as in Fig. 3c).

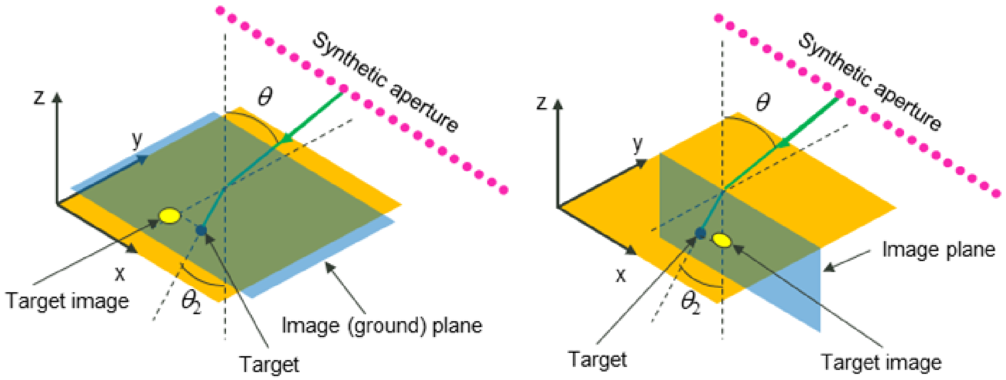

(a) (b)

Fig. 2 Diagrams showing two possible imaging modes of a side-looking GPR system: a) horizontal ground plane imaging; b) vertical plane imaging

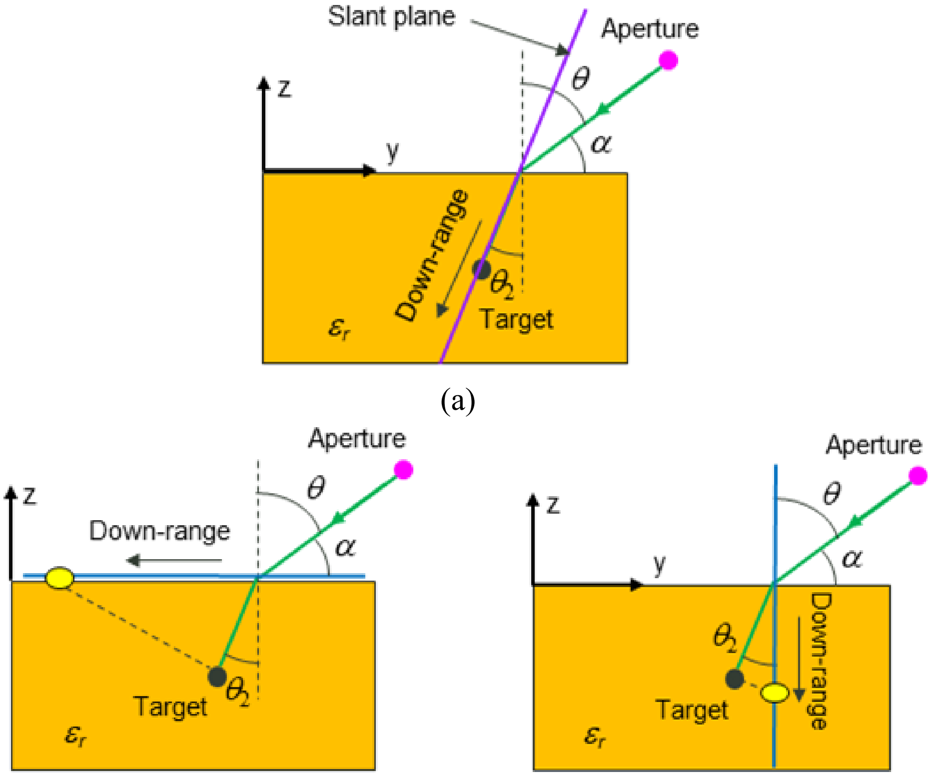

(a)

(b) (c)

Fig. 3 Diagram of a side-looking GPR system, showing the downrange direction for three imaging modes: a) slant image plane; b) horizontal image plane; c) vertical image plane

In the actual image planes, the downrange resolution must be adjusted by the factor $\frac{1}{\cos\beta}$, where β is the angle between the slant and image planes. This resolution is

$$\delta y = \frac{c}{2B\cos\alpha} \text{ for horizontal plane,} \tag{1a}$$

$$\delta z = \frac{c}{2B\sqrt{\varepsilon_r}\cos\theta_2} = \frac{c}{2B\sqrt{\varepsilon_r - \cos^2\alpha}} \text{ for vertical plane.} \tag{1b}$$

In these equations, c is the speed of light, B is the radar signal bandwidth, ε_r is the ground dielectric constant, and α is the incidence (or depression) angle measured with respect to the ground plane (as in Fig. 1). In all our numeric simulations, we work with ultra-wideband (UWB) radar waveforms typical for this application, with a frequency spectrum ranging from 0.5 to 2 GHz.

Comparing the resolutions given by Equations 1a and 1b, we see that the ratio between the vertical- and horizontal-plane image downrange resolutions is $\tan\theta_2 = \frac{\cos\alpha}{\sqrt{\varepsilon_r - \cos^2\alpha}}$. The factor $\tan\theta_2$ reaches a maximum of $\frac{1}{\sqrt{\varepsilon_r - 1}}$ (when $\alpha =$ 0°), which is always smaller than unity for any type of soil; this means, the vertical plane image downrange resolution is always better than the horizontal plane counterpart. A simple, intuitive justification for this statement is that the slant plane orientation is closer to the vertical than the horizontal plane, as dictated by Snell's law propagation angles.[11]

The cross-range resolution (along the x-axis) is the same in both cases (horizontal and vertical image planes) and given by

$$\delta x = \frac{\lambda_c R}{2L_x}, \tag{2}$$

where λ_c is the wavelength at the center frequency of the radar signal, R is the radar-pixel range (more exactly, the propagation path length from the aperture center to the pixel) and L_x is the aperture length. As shown elsewhere,[2] the cross-range resolution has a lower limit of $\frac{\lambda_c}{4}$.

In Section 2.2 we analyze the PSF, which is the imaging system's response to a point target. These models are created via analytic formulas established elsewhere.[1] In Sections 3 and 4 we evaluate the radar clutter, more specifically clutter produced by the rough ground surface and the soil dielectric inhomogeneities. To estimate the TCR, we need to calibrate the radar target response to that of a realistic target, relevant to CEH applications. For this purpose, we employed the signature of a flush-buried M15 antitank landmine, obtained by computer simulations.

Modeling the radar wave propagation and scattering in the presence of the landmine, rough surface, or inhomogeneous ground was performed using the AFDTD software,[12,13] developed at DEVCOM ARL and described in several previous publications. Since these represented very large-scale simulations, the computations were carried out on high-performance computing (HPC) platforms available at the DOD HPC Centers.[14]

The antennas used in the AFDTD simulations are infinitesimal dipoles, oriented in the *x* direction for horizontal polarization, or in the *z* direction for vertical polarization. The same type of antenna is used both as Tx and Rx, yielding either H-H or V-V polarization combinations for the radar system. A further discussion of this antenna implementation was presented in a previous report and is not repeated here.[4]

The frequency-domain scattered field data obtained from AFDTD simulations are fed into an image formation algorithm, effectively simulating a stepped-frequency UWB radar. The imaging algorithm is based on the matched filter method,[5] which is the frequency-domain equivalent of the well-known backprojection algorithm. Formally, the image formation algorithm is described by the following equation:

$$I\left(\mathbf{r}\right)=\frac{1}{NM}\sum_{n=1}^{N}\sum_{m=1}^{M}W\left(f_n,\mathbf{r}_m\right)P\left(f_n,\mathbf{r}_m\right)\exp\left(j\frac{4\pi f_n}{c}R_m\right), \tag{3}$$

where f_n stands for the frequency index n; $\mathbf{r}_m$ is the position vector of the radar at aperture sample index m; R_m is the radar-pixel propagation path length; $I\left(\mathbf{r}\right)$ is the complex image pixel amplitude at position vector $\mathbf{r}$; $P\left(f_n,\mathbf{r}_m\right)$ is the radar signal obtained at aperture sample index m and frequency index n; N stands for the number of frequencies; and M stands for the number of aperture samples. In most scenarios, tapered windows $W\left(f_n,\mathbf{r}_m\right)$ were applied to the radar data in the frequency and aperture dimensions, for sidelobe control. Equation 3 assumes a monostatic radar configuration. For additional details, such as the calculation of R_m, see Dogaru.[1]

One important feature in down-looking GPR images is the strong reflection from the air–ground interface (the "ground bounce"). As discussed elsewhere,[4] the ground bounce can be at least partly mitigated by subtracting the coherent average of the radar signals along the synthetic aperture from the radar data. This eliminates the signal reflected from a flat interface between air and homogeneous ground, but does not reduce the scattering from various random clutter sources, such as rough surface or soil permittivity fluctuations. As is well-known, side-looking SAR geometries are less impacted by the ground bounce issue, since the specular reflection from the air–ground interface propagates away from the radar Rx. Nevertheless, to ensure that no remnants of the ground bounce show up in the side-looking GPR images (which is a still distinct possibility in very-near-range sensing geometries), we always perform the average signal subtraction before creating the images in this report.

2.2 Point Spread Function of the Side-Looking GPR Imaging System

Investigating the PSF of a side-looking GPR imaging system for every possible configuration is beyond the scope of this report. Only a few numerical examples are presented in this section, with the purpose of elucidating some important phenomenological aspects relevant to this sensing modality. One crucial distinction in 2-D imaging with side-looking GPR is that between targets located in the image plane and those located outside the image plane. This issue was already discussed in one of our previous reports, in the context of down-looking GPR.[4] However, the current work goes into further details of this problem with deep implications on the side-looking GPR sensing mode.

As is well-known in radar imaging theory, employing a linear aperture allows resolving targets in only two spatial dimensions, or creating 2-D images. That means the target is not resolved in the third spatial dimension. In other words, we would not be able to precisely localize a target in the 3-D space with an imaging radar equipped with a linear aperture: in the 3-D space, the target image will appear smeared along a curve or surface, which we call the "ambiguity curve/surface". This ambiguity curve/surface is perpendicular to the slant plane, with the mention that the slant plane orientation also changes with the target position.

When we create a 2-D radar image in the presence of a target, we obtain the intersection of the ambiguity surface with the image plane. If the target is placed in the image plane to start with, then its image is well focused and shows at the correct coordinates in that plane. If the target is placed outside the image plane, then its image becomes defocused and appears at wrong spatial coordinates. To illustrate these statements, we consider two numerical examples involving point targets.

In the first example we consider a point target in the ground plane, at coordinates $\left(0,-1,0\right)$ m. The linear aperture is placed at height h = 1 m and ground range R_g = 1 m (measured from the origin), and has length L_x = 4 m. The air–ground interface is always located at the z = 0 coordinate. As in all numerical examples in this report, the radar frequency band goes from 0.5 to 2 GHz, while the ground has the following dielectric properties: $\varepsilon_r = 5$, $\sigma = 0.02$ S/m. The radar operates in H-H polarization. Hanning windows are applied to the radar data in both frequency and aperture dimensions. In Fig. 4, we show the 2-D images obtained in the $z = 0$ (or ground) horizontal plane (Fig. 4a) and the $y = –0.5$ m vertical plane (Fig. 4b), together with a 3-D view that adds the $x = 0$ vertical plane image to the other two planes already mentioned (Fig. 4c).

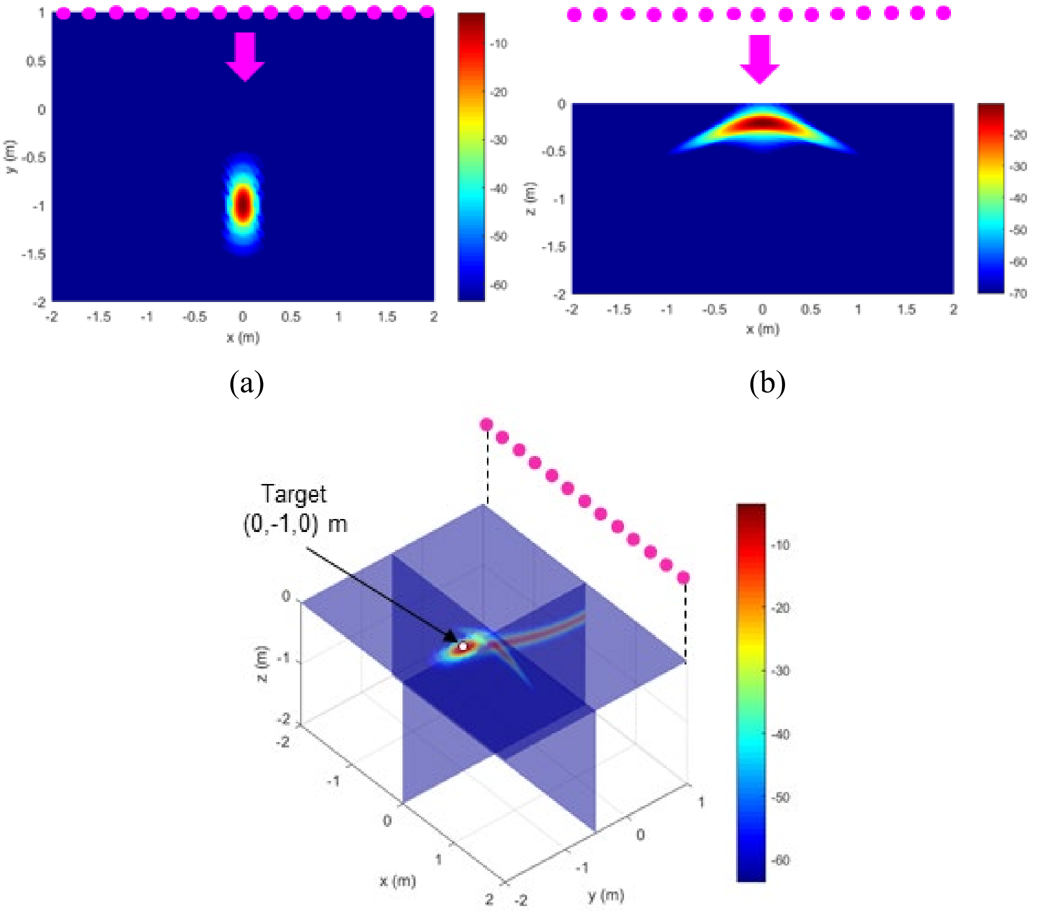

(a)

(b)

(c)

Fig. 4 PSF of a target placed at coordinates (0,–1,0) m obtained with a very short range side-looking GPR system, showing a) the 2-D image in the horizontal z = 0 plane; b) the 2-D image in the vertical y = –0.5 m plane; and c) 3-D view of the images obtained in the x = 0, y = –0.5 m, and z = 0 planes. The pink dots represent the synthetic aperture sample positions, while the pink arrows indicate the downrange directions in the 2-D images.

The horizontal plane image (Fig. 4a) contains the target, which appears well focused at the correct (x, y) coordinates. The PSF resolutions in the two directions can be evaluated via the formulas in Eqs. 1a and 2. However, the image in the vertical plane (Fig. 4b), which does not contain the target, clearly appears out of focus, with the center of the image at the wrong z coordinate (–0.2 m instead of 0 m).

In the second example we place the point target at coordinates $(0, -0.5, -0.5)$ m and create 2-D images in the same planes ($z = 0$ and $y = -0.5$ m, respectively). All the radar parameters (frequencies and aperture geometry) are identical to the previous example. In Fig. 5a we show the $z = 0$ horizontal plane image, while in Fig. 5b we show the vertical plane image. Now the target is out of the horizontal image plane and appears defocused (Fig. 5a). Additionally, the y coordinate in the image center is completely off (–1.6 m instead of –0.5 m). On the other hand, the target is properly focused and positioned in the vertical plane image, which contains the target location. In this case, the PSF resolutions in the x and z directions can be evaluated by the formulas in Eqs. 1b and 2.

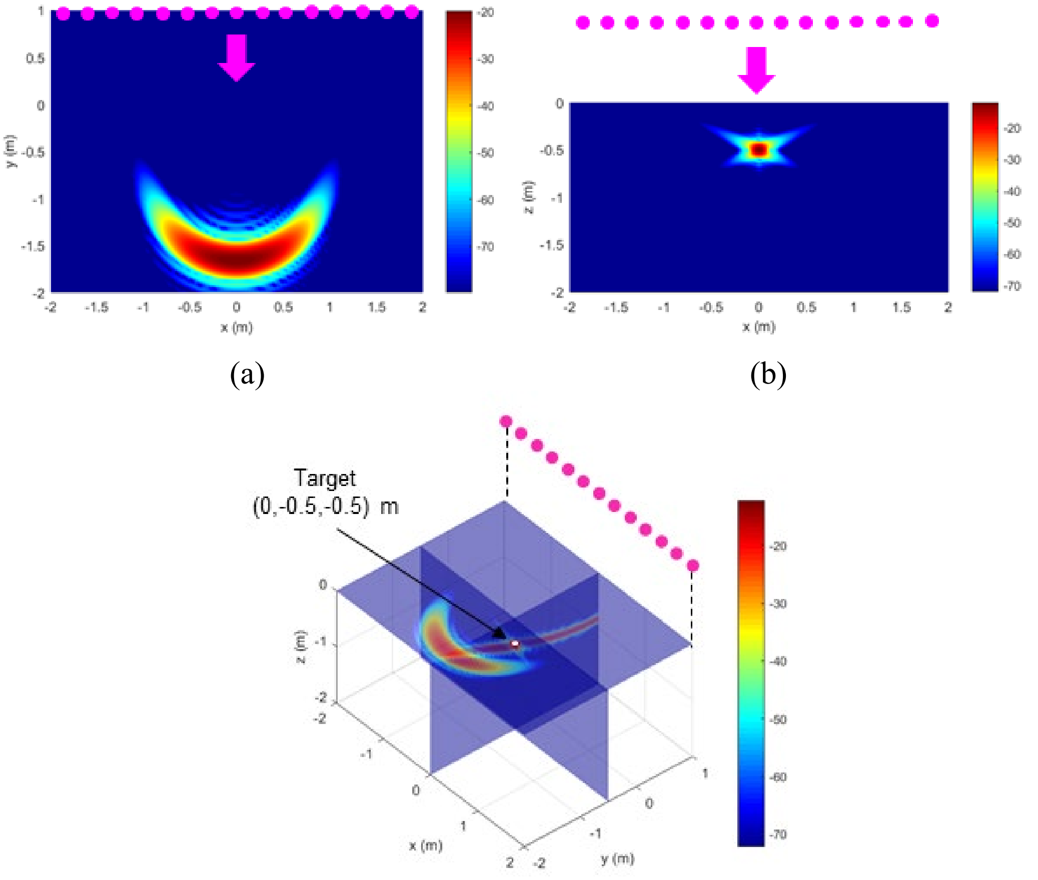

(a) (b)

(c)

Fig. 5 PSF of a target placed at coordinates (0,–0.5,–0.5) m obtained with a very short range side-looking GPR system, showing a) the 2-D image in the horizontal z = 0 plane; b) the 2-D image in the vertical y = –0.5 m plane; and c) 3-D view of the images obtained in the x = 0, y = –0.5 m and z = 0 planes. The pink dots represent the synthetic aperture sample positions, while the pink arrows indicate the downrange directions in the 2-D images.

The defocusing and wrong localization of the target in out-of-plane images are clearly detrimental to the radar system's performance. As seen in the previous numerical examples, the target image peak magnitude can drop by about 10 dB with respect to the in-plane image, with negative effect on detection performance. Additionally, the defocusing leads to a loss of resolution that makes the target's spatial separation from other targets or clutter items more difficult. Since we typically do not have any a priori information on the target location, choosing the correct imaging plane for maximum radar performance cannot be done in a deterministic fashion. One possible solution to this problem is to create multiple images in several parallel planes (horizontal or vertical) within a certain spatial region and pick the one displaying the best-focused target image. In any case, it now becomes clear that forming the GPR image of buried targets in the ground plane is suboptimal, since in that case the target is placed out of the image plane.

The previous numerical examples are somewhat extreme and not very representative for side-looking GPR geometries, in the sense that the radar–target range is very short. This leads to a large degree of target defocusing (measured by the cross-range image spread), as well as a large drop in peak image magnitude. A more representative scenario for this sensing mode places the radar at longer range from the imaging area. (Note: Throughout this report, we label the case where $R_g \geq 3.8$ m as "medium range"; this designation is relative to the very-short-range scenario where $R_g = 1$ m, although, in absolute terms, all the ranges considered here are very short for a radar system.) Two additional numerical examples illustrate this case.

Figure 6 shows the images of a target placed at coordinates $\left(0, -1, 0\right)$ m, obtained with a linear-track SAR placed at $h = 1.6$ m and $R_g = 3.8$ m. The aperture length in this case is $L_x = 7.6$ m, with all the other radar parameters identical to the previous examples. The aperture integration angle in this scenario is about the same as in the sensing geometry employed in the previous two numerical examples. Figure 6a displays the 2-D image in the horizontal ground plane ($z = 0$), where the target is well focused, while Fig. 6b shows the image in the vertical ground plane ($y = -0.5$ m), which is offset with respect to the target coordinates. Both the defocusing degree and the magnitude drop in the latter image are similar to those in Fig. 4.

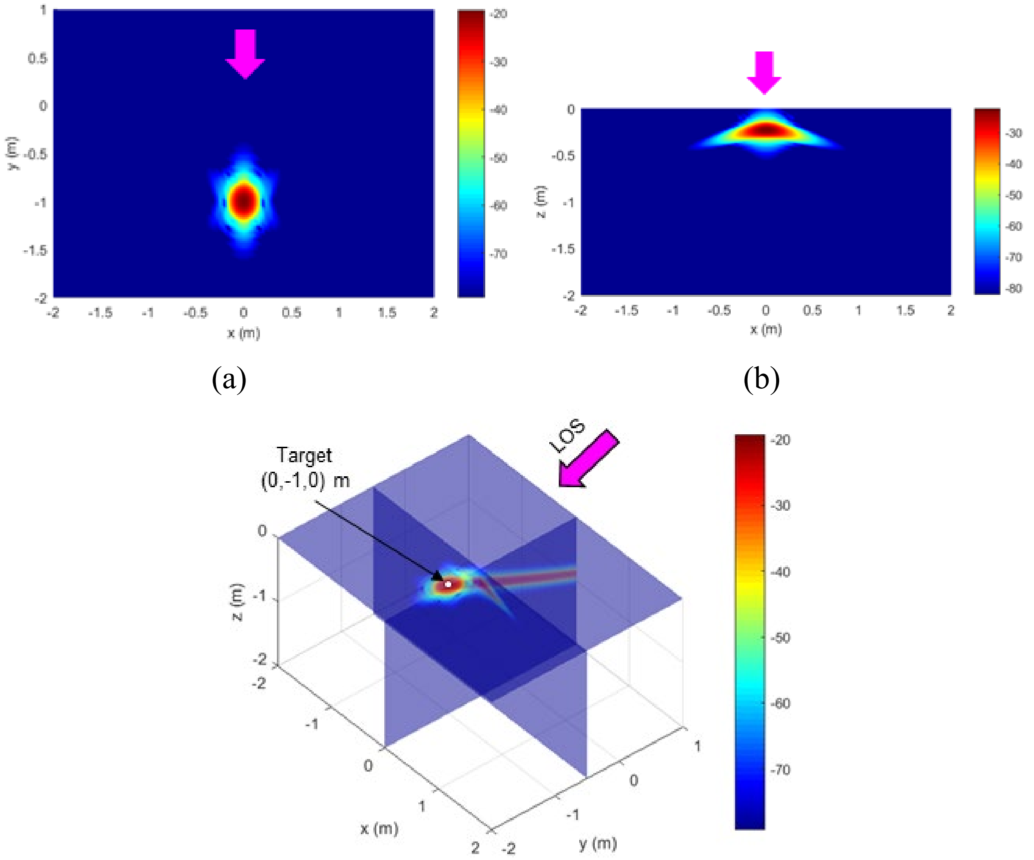

(a)

(b)

(c)

Fig. 6 PSF of a target placed at coordinates (0,–1,0) m obtained with a medium-range side-looking GPR system, showing a) the 2-D image in the horizontal z = 0 plane; b) the 2-D image in the vertical y = –0.5 m plane; and c) 3-D view of the images obtained in the x = 0, y = –0.5 m and z = 0 planes. The pink arrows indicate the downrange directions in the 2-D images (a and b) or the radar LOS in the 3-D view (c).

Figure 7 examines a similar scenario in terms of radar geometry and parameters, but with the target placed at coordinates $(0,-0.5,-0.5)$ m. The out-of-plane image in Fig. 7a displays a degree of defocusing comparable to that in Fig. 5a. The similarity between the images obtained in the scenarios presented in Figs. 4 and 5, on one hand, and those in Figs. 6 and 7, on the other hand, suggests that the amount of target defocusing depends primarily on the aperture integration angle rather than the radar–target range. This finding is consistent with results obtained in Section 3 and is explained in more detail in the Appendix.

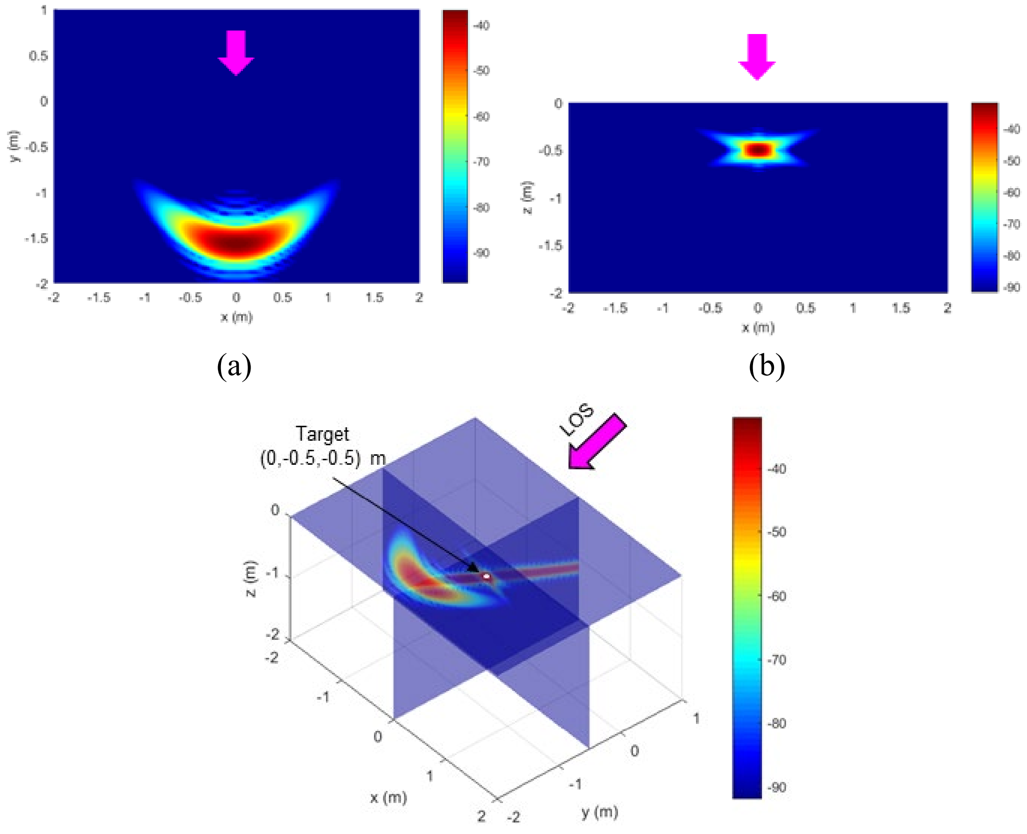

(a) (b)

(c)

Fig. 7 PSF of a target placed at coordinates (0,–0.5,–0.5) m obtained with a medium range side-looking GPR system, showing a) the 2-D image in the horizontal z = 0 plane; b) the 2-D image in the vertical y = –0.5 m plane; and c) 3-D view of the images obtained in the x = 0, y = –0.5 m and z = 0 planes. The pink arrows indicate the downrange directions in the 2-D images (a and b) or the radar LOS in the 3-D view (c).

Besides the defocusing effects on the target image, the out-of-plane imaging issue plays a very important role in imaging the clutter with a side-looking GPR sensor. This aspect is analyzed in detail in Section 2.3. Before concluding the current section on the point target signature, we look at its magnitude variation with burial depth in the GPR image. The imaging scenario is identical to that considered in the Fig. 6 example. The target is placed at coordinates $x_0 = 0$, $y_0 = 0$ and $z_0 = -d$, where the depth d varies from 0 to 1 m. The peak magnitude in the image is calibrated to equal that of the image of a flush-buried M15 metal antitank landmine at $d = 0$, with exactly the same radar parameters as in the point target imaging scenario. The peak power of the calibrated PSF (in short, "the target power") as a function of depth, for both H-H and V-V polarizations, is plotted in Fig. 8.

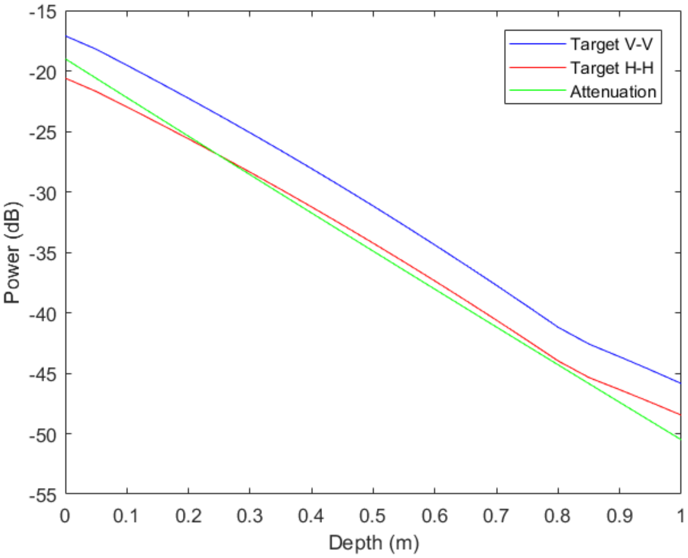

Fig. 8 Variation of the point target power in the side-looking GPR images (PSF peak) as a function of burial depth, plotted together with the two-way wave attenuation in the ground medium

In the same figure we added a plot of the two-way attenuation of the radar wave in the ground medium. Since the target response and attenuation curve have almost the same slope, we infer that the reduction in the target image magnitude with increasing depth can be almost entirely attributed to the radar wave attenuation in the lossy propagation medium. The same result was consistently obtained in multiple simulations with various radar geometry parameters, including those presented in Section 3, as well as in the down-looking scenarios investigated in our previous work.[4] For reference, the two-way magnitude attenuation formula, assuming small loss tangent of the ground is

$$Atten^{2-way} = \exp\left(-\frac{Z_0 \sigma}{\sqrt{\varepsilon_r - \dfrac{R_g^2}{h^2 + R_g^2}}} d \right), \tag{4}$$

where Z_0 is the free-space impedance, and σ is the conductivity of the soil.

2.3 Out-of-Plane Clutter Imaging Issues in Side-Looking GPR

The out-of-plane imaging issue, described in the previous section in relation to point target images, plays a very important role in the clutter appearance in GPR images as well. This problem has been investigated in a previous report,[4] where we showed that the rough surface clutter extends much deeper than its physical location in a down-looking GPR image. In this section, we expand that analysis to side-looking GPR sensing scenarios.

When we create a side-looking SAR image in the horizontal ground plane, the rough surface is physically located in the image plane and the clutter appears across the entire image. Multiple tools have been developed to analyze the clutter in this traditional SAR imaging mode[15] (some of those are described in Section 3). However, not much attention has been devoted to the impact of rough surface clutter onto underground images obtained with GPR systems. In down-looking GPR, all the rough surface scattering centers located within the antenna beam footprint project along the ambiguity curves/surfaces onto the vertical image plane; therefore, the image clutter has strong power at relatively large depths.[4]

A similar effect takes place in vertical-plane underground images obtained with side-looking GPR as well. However, the issue is typically more severe in side- than in down-looking sensing configurations, for two reasons: 1) the antenna beam footprint on the ground is wider than in the down-looking case, due to the slanted incidence plane geometry, and 2) for normal operational ranges, the ambiguity curves become straight lines whose intersections with the vertical image plane extend deep underground. Moreover, scattering produced by clutter objects placed *above* the ground plane (e.g., bushes, trees, or other vegetation items) is also projected along ambiguity curves/surfaces and has an impact on the same underground images. The sensing scenario we have in mind for the phenomenological analysis in this section is illustrated in Fig. 9.

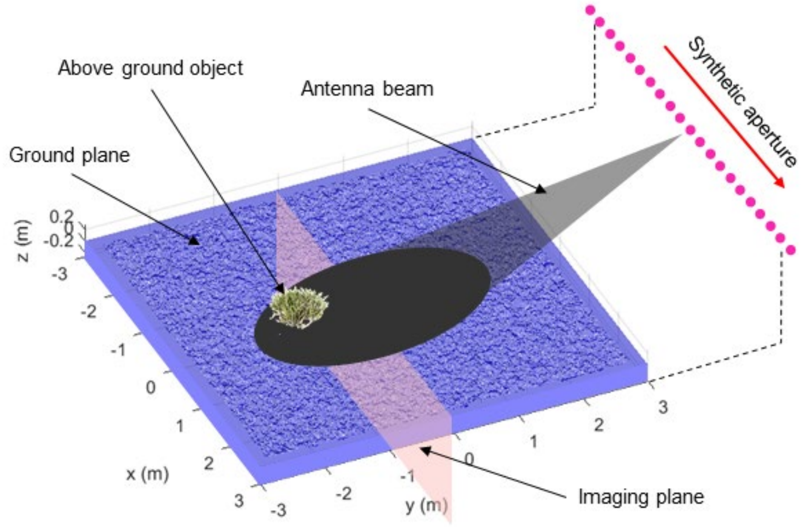

Fig. 9 Diagram of a side-looking GPR imaging system showing rough surface and aboveground discrete clutter objects, with the image created in a vertical underground plane

We defer the quantitative numerical evaluation of clutter in side-looking GPR images to Sections 3 and 4. In the current section, we emphasize some qualitative aspects of the rough surface and above-surface clutter impact on underground images.

A first numerical example is presented in Fig. 10, which simulates the image obtained in the presence of three point targets placed at the air–ground interface, with these points representing scattering centers from the rough ground surface. The points are placed at coordinates $\left(0,-1,0\right)$ m, $\left(0,0,0\right)$ m, and $\left(0,1,0\right)$ m, respectively. The radar geometry (different from the scenarios in Section 2.2) involves a ground range $R_g = 10$ m and a height $h = 5$ m, both measured from the origin (as a reminder, the air–ground interface is always located at $z = 0$). The synthetic aperture length is $L_x = 8$ m, which yields a significantly smaller integration angle than the configurations investigated in Section 2.2.

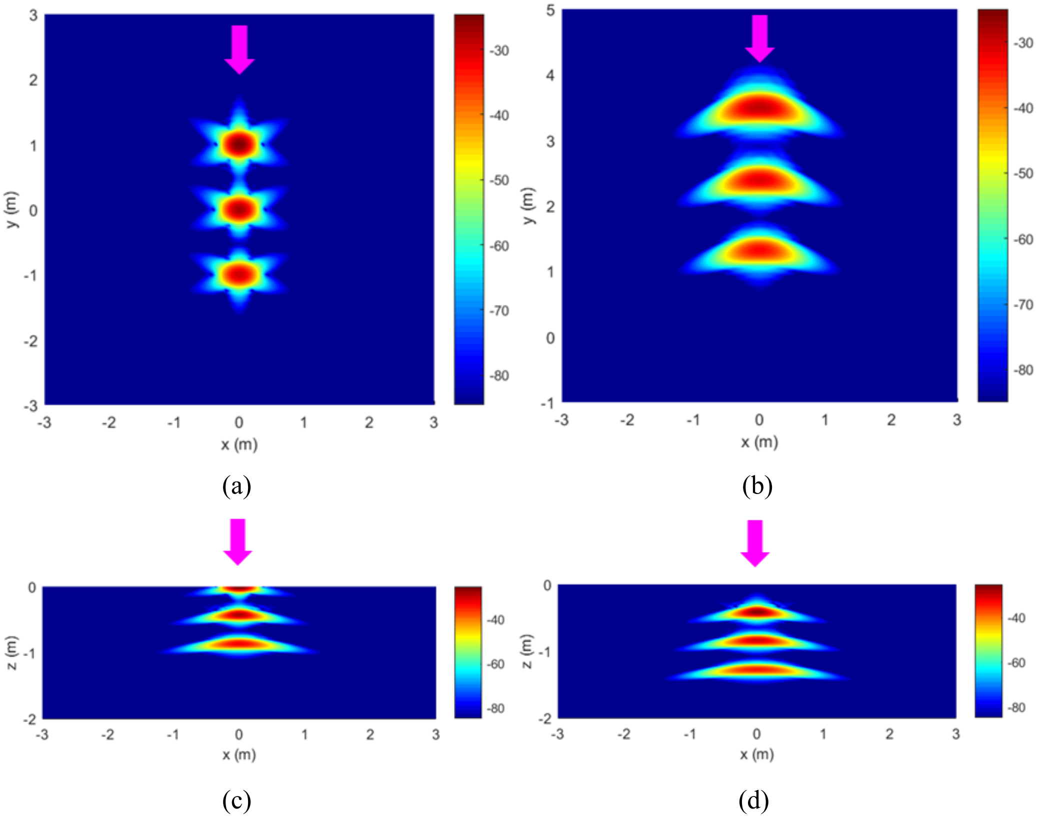

(a) (b)

(c) (d)

Fig. 10 Image of three point targets placed at the air–ground interface, obtained with the side-looking GPR system, represented in the following planes: a) z = 0; b) z = –1 m; c) y = 1 m; d) y = 2 m; e) x = 0; and f) 3-D view of the images in the z = 0, y = 1 m, and x = 0 planes. The pink arrows represent the downrange directions (a–d) or the radar LOS (e and f). The white dashed lines in e) show the positions of the image planes used in a–d).

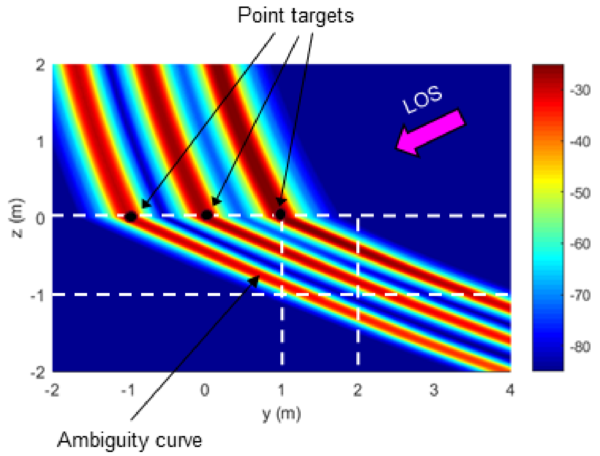

(e)

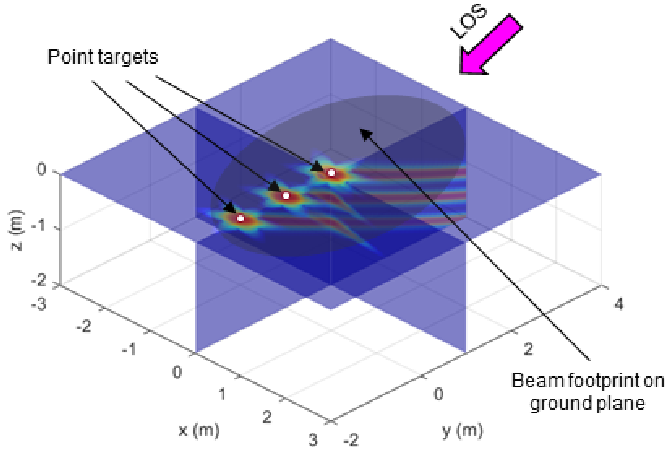

(f)

Fig. 10 Image of three point targets placed at the air–ground interface, obtained with the side-looking GPR system, represented in the following planes: a) z = 0; b) z = –1 m; c) y = 1 m; d) y = 2 m; e) x = 0; and f) 3-D view of the images in the z = 0, y = 1 m, and x = 0 planes. The pink arrows represent the downrange directions (a–d) or the radar LOS (e and f). The white dashed lines in e) show the positions of the image planes used in a–d) (continued).

For this case, we included two horizontal plane images (z = 0 in Fig. 10a and z = –1 m in Fig. 10b) and two vertical image planes (y = 1 m in Fig. 10c and y = 2 m in Fig. 10d). For z = 0, the targets are located in the image plane and well focused. For z = –1 m, we have to deal with out-of-plane targets, which appear defocused. Two of the images in the y = 1 m vertical plane (Fig. 10c) are also defocused, since those targets are again placed outside the image plane. As we move the vertical image plane farther away from the true target locations, as in Fig. 10d, we notice a larger amount of image defocusing (spread in the x direction). This example proves that the out-of-plane defocusing issue affects both horizontal and vertical plane images. However, the degree of defocusing is not as pronounced as in the numerical examples in Section 2.2 (Figs. 4–7), due to the smaller integration angle for the current sensing geometry.

Fig. 10e represents the 2-D image obtained in the vertical plane $x = 0$ and clearly shows the ambiguity curves in this plane. We extended this image in a region above the ground plane as well ($z > 0$). In this region, the ambiguity curves are circles centered at the (y, z) coordinates of the aperture that go through the target location. In the region underground ($z < 0$), the ambiguity curves look almost like straight lines within the limited image extent. The discontinuity in the ambiguity curve slopes at the air–ground interface mirrors the change in radar wave propagation direction at the same interface due to refraction. The image defocusing, manifested as smearing in the cross-range direction, is present only in the underground part of the image, but not in the aboveground region. A more detailed analysis of the ambiguity curves and surfaces is presented in the Appendix.

In the next numerical example we consider a point target above the ground plane, corresponding to a clutter item located in that region of the space. As a preliminary, we offer a simple explanation of the scattering phenomenology of that point target. There are four possible backscattering mechanisms from the target in the presence of the ground plane, involving the direct and ground-reflected propagation paths between the radar and target: direct-direct, direct-reflected, reflected-direct, and reflected-reflected (see Fig. 11). The direct-reflected and reflected-direct propagation mechanisms yield identical signal phases, so they can be lumped together into one signal of double magnitude. Consequently, we expect to obtain three radar images of the target, one corresponding to each distinct propagation mechanism.

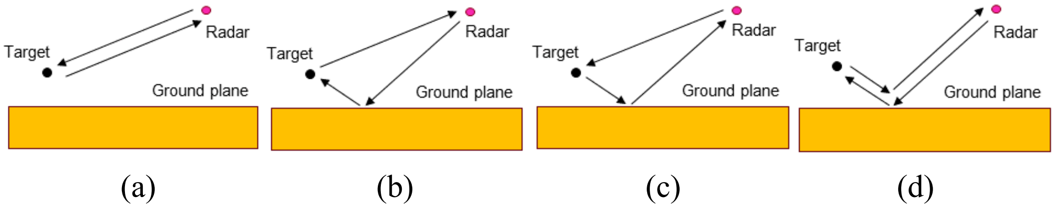

Fig. 11 Diagram of the four backscattering mechanisms involved in the radar response of a point target placed above the ground plane: a) direct-direct; b) reflected-direct; c) direct-reflected; and d) reflected-reflected

This is indeed the case in Fig. 12, where we represent the images generated by a point target placed at $(0, -1, 0.5)$ m, with the same radar parameters as in the previous example. This simulation is representative for a clutter object placed above the ground plane. As seen in Figs. 12a and b, the aboveground clutter has an impact on underground images, due to its projections along the ambiguity curves.

In each 2-D image plane, a set of three images is generated by the single point target. The spatial separation between these images increases with the target height. The high resolution in this simulation enables distinguishing the three separate images; however, in most experimental data, where we deal with more complex-shaped objects of larger extent usually placed close to the ground plane, the three propagation mechanisms originating from one scattering center are very difficult to separate and typically show as one single image.

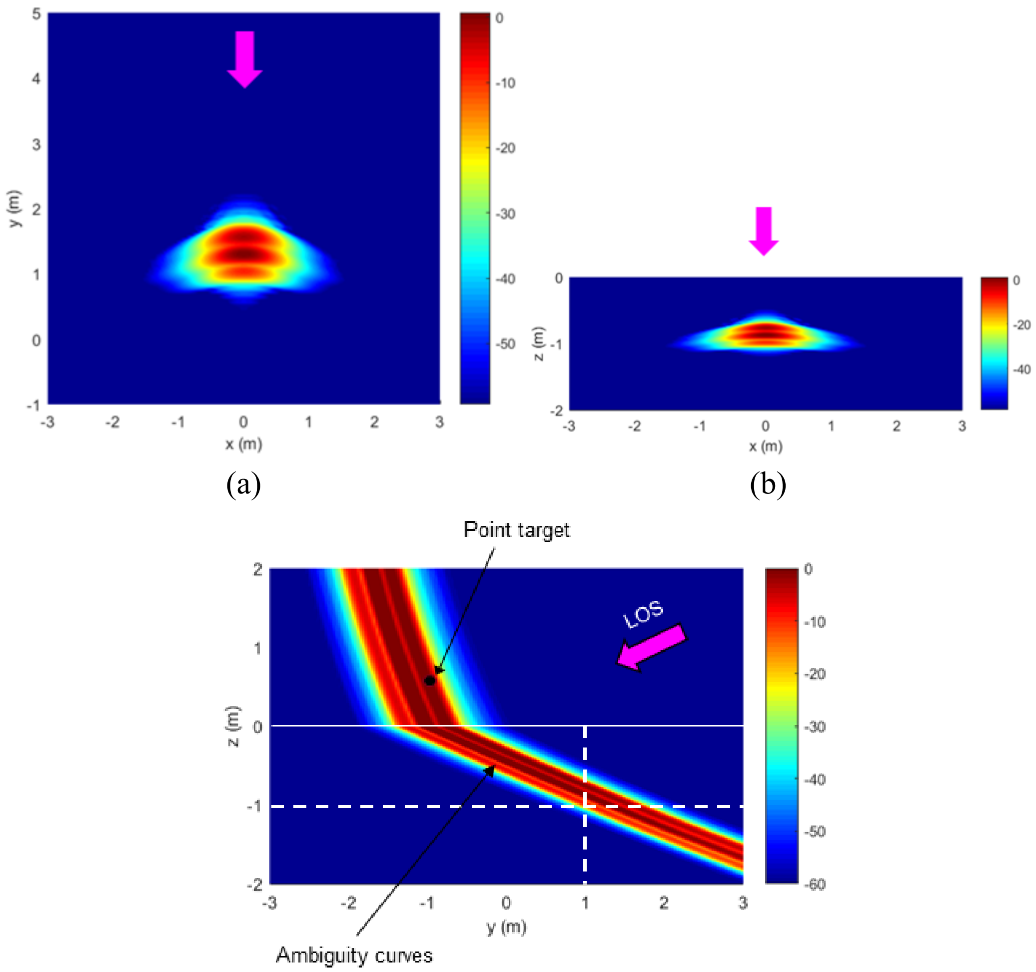

(a)

(b)

(c)

Fig. 12 Image of a point target placed above the ground plane, obtained with the side-looking GPR system, represented in the following planes: a) z = –1 m; b) y = 1 m; and c) x = 0. The pink arrows represent the downrange directions (a and b) or the radar LOS (c). The white dashed lines in c) show the positions of the image planes used in a and b).

One key aspect of the clutter impact onto a 2-D underground image is the small amount of attenuation the projections generated by above- or on-surface scattering centers incur along the ambiguity curves. For instance, in the images shown in Figs. 10 and 12, the magnitude drop is only about 5 dB between the ground-plane and the $z = -1$ m-plane images. This effect is coupled with the approximately straight-line shape of the ambiguity curves, which guarantees deep penetration of these projections into the underground space. Crucially, the projection magnitude reduction has nothing to do with the radar wave attenuation in the lossy dielectric medium, but is only dictated by the amount of image defocusing. This relatively strong underground clutter projection eventually competes with the true buried target image, which in turn experiences severe attenuation due to dielectric losses in the ground. This qualitative phenomenological explanation underscores the significant challenge in detecting deep-buried targets with a side-looking GPR imaging system.

3. Rough Surface Clutter in Side-Looking GPR Imaging

In this section, we present a quantitative analysis of rough surface clutter in side-looking GPR imaging scenarios, with the final goal of evaluating the TCR, which is the first indicator of radar detection performance. In particular, we are interested in studying the TCR variation with certain parameters of the sensing geometry (angle of incidence, platform range and height, target burial depth), for the purpose of optimizing the radar system operation. We start by investigating far-field sensing configurations, which have the advantage of allowing a clear-cut definition of the radar cross section (RCS), as well as the analytic estimation of the rough surface clutter mean power. Subsequently, we discuss the qualitative differences presented by near-range sensing scenarios by way of numerical examples.

3.1 Far-Field Image Analysis

Far-field imaging scenarios are typically associated with long-range, airborne radar sensors, flying at relatively high altitude. The sensing geometry of a low-flying UAV-based radar system typically does not conform to the far-field model. Nevertheless, it is interesting to consider radar images generated by this model, due to the availability of powerful far-field analysis tools for both target and clutter radar signature, which allow the rapid evaluation of the TCR for a wide range of sensing parameters.

As a reminder, the far-field imaging scenarios involve plane-wave propagation of the radar waves across the image domain. This propagation is characterized by a set of azimuth and elevation angles, whereas the radar range does not play a role in some measurements (e.g., RCS evaluation). In this case, the image formation algorithm must take into account the planar nature of the wave fronts, in contrast with the near-field radar imaging scenarios, characterized by propagation of spherical wave fronts. Although the far-field assumption is an idealization of the true radar propagation scenario, it allows a number of approximations that are widely used in radar system analysis. For instance, the important concept of target RCS can only be precisely defined in the far-field case.[5] Another powerful concept that is only rigorously valid in the far-field is the mean RCS per unit area (denoted σ^0), used to characterize the radar signature of distributed random clutter.[15,16]

The image formation algorithm based on the matched filter method must be modified for the far-field as follows:

$$\begin{gathered}
I(x,y,z)=\frac{1}{NM}\sum_{n=1}^{N}\sum_{m=1}^{M}P(f_n,R_m,\phi_m,\theta_m)\times \\
\exp\left(j\frac{4\pi f_n}{c}\left(R_m-\left(x\cos\phi_m\sin\theta_m+y\sin\phi_m\sin\theta_m+z\sqrt{\varepsilon_r-\sin^2\theta_m}\right)\right)\right)
\end{gathered}. \quad (5)$$

In this equation, (x,y,z) are the pixel coordinates, whereas (R_m,ϕ_m,θ_m) are the radar spherical coordinates at the aperture sample index m, with all these coordinates referenced to an origin placed in the ground plane, within the image region. This equation is valid for both above- and underground image pixels; for aboveground pixels, we simply set $\varepsilon_r = 1$.

Far-field SAR imaging scenarios involving a linear aperture lead to similar issues related to out-of-image-plane targets as those discussed in Section 2 of this report, including image defocusing and loss of magnitude. The ambiguity curves become straight lines perpendicular to the direction of propagation, while the ambiguity surfaces get wider as we move away from the target location. This widening is proportional to the integration angle, which confirms the fact that the amount of defocusing is dictated by the size of the integration angle rather than the radar–target range.

When considering the effect of rough surface clutter on the underground radar images, we take into account the projection of the returns from scattering centers located at the air–ground interface along the ambiguity curves and surfaces, in a manner similar to the down-looking GPR analysis performed in our previous work.[4] To illustrate this issue, in this section we present the results of a simulation involving the far-field imaging of a rough surface with a SAR system operating with a linear aperture along the x-axis. The frequency band extends from 0.5 to 2 GHz, the integration angle is 60°, while the incidence angle in the aperture center is α = 45°. (As a reminder, in this report, by incidence angle we imply the depression angle α, measured from the horizontal plane, which is the complement of the elevation angle θ, measured from the vertical. All the subsequent graphs and equations use the depression angle α.)

The rough surface is characterized by the root mean square (RMS) height h_{RMS} = 5 mm and the correlation length L_c = 5 cm. The 2-D surface height $z(x,y)$ is modeled as a stationary random process with exponential covariance function given by the following expression:

$$C_z(x,y) = h_{RMS}^2 \exp\left(-\frac{2\sqrt{x^2+y^2}}{L_c}\right). \tag{6}$$

When expressed in polar coordinates of the *x-y* plane, the covariance function in this model does not depend on the azimuth angle, but only on the horizontal displacement $\rho = \sqrt{x^2+y^2}$. The spectral power density of this surface, which is the 2-D Fourier transform of the covariance function, follows a power-law expression given by

$$W(k_x,k_y) = \frac{\pi h_{RMS}^2 L_c^2}{2\left(1+\frac{(k_x^2+k_y^2)L_c^2}{4}\right)^{\frac{3}{2}}}, \tag{7}$$

where (k_x,k_y) are the Fourier domain counterpart of (x,y). Again, the spectrum depends only on the magnitude of the wave vector's horizontal component, $k_\rho = \sqrt{k_x^2+k_y^2}$.

The radar wave propagation and scattering from the rough surface were simulated with the AFDTD electromagnetic (EM) modeling software. The ground has the same dielectric properties as in the Section 2 simulations. The modeling software can only accommodate a finite rough surface patch, which in our simulation has a size of approximately 4 m (in the *x* direction) by 8 m (in the *y* direction). One could interpret this limited extent of the clutter-generating rough surface as a consequence of the finite antenna beam footprint on the ground plane. However, this interpretation is incorrect in far-field sensing scenarios, where the incident plane wave is supposed to illuminate a surface of infinite size. This model limitation must be taken into account when evaluating the mean clutter power in the radar images.

The imaging results in three principal planes (z = 0, y = 3 m, and x = 0) for H-H polarization are shown in Fig. 13. No windowing was applied to the radar data in either frequency or aperture dimension. The horizontal-plane image in Fig. 13a clearly shows the finite extent of the simulated rough surface patch. The ambiguity curves can be seen in Fig. 13c: they are straight lines perpendicular to the propagation direction inside the ground medium (which, according to Snell's law, makes an 18° angle with the vertical). These ambiguity curves terminate rather abruptly at the two rough surface ends in the *y* direction. This is obviously an artifact generated by the finite rough surface extent, as explained in the previous paragraph. In reality, the rough surface should extend indefinitely in the *y* direction, and the ambiguity curves should fill the entire underground space. To circumvent this limitation of the model, for the *x-z* plane image we chose the *y* = 3 m vertical plane, where the rough surface projections fill out the entire image down to a depth of 2 m.

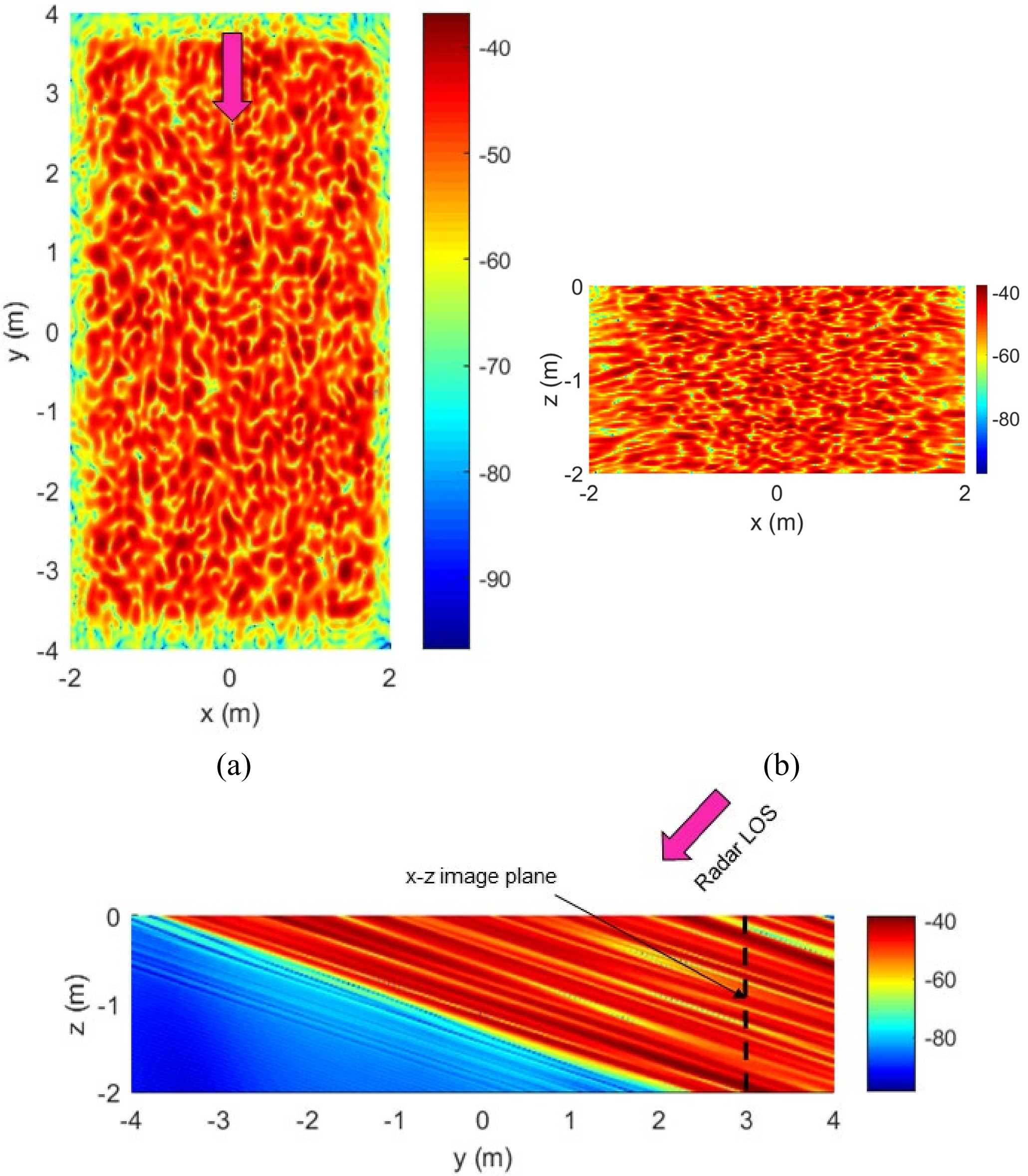

(a) (b)

(c)

Fig. 13 2-D images of rough surface clutter, for far-field sensing at 45° incidence, created in the following planes: a) z = 0; b) y = 3 m; and c) x = 0. The arrows indicate the radar look direction, or LOS.

The main parameter we are interested in extracting from the images in Fig. 13 is the mean pixel power. As reference we use Fig. 13a, which represents the conventional ground-plane imaging geometry of side-looking SAR systems. In this scenario, where the scattering centers are actually located in the image plane, the mean pixel power is –41 dB for V-V polarization and –46 dB for H-H polarization. When we evaluate the same metric in the vertical-plane image in Fig. 13b, we obtain exactly the same numbers as in the ground plane. Moreover, the numerical experiments show that the same mean pixel power characterizing the rough surface clutter is obtained in any horizontal (*x*-*y*) or vertical (*x*-*z*) image planes, regardless of whether the scattering centers are located inside or outside those planes. That means, despite the defocusing caused by the out-of-plane imaging issue, when averaged out across the entire image, the rough surface clutter shows up with the same mean power in both horizontal and vertical image planes. Another observation is that the mean clutter power is uniform across the image for the finite extent of the rough surface patch. This holds true for both horizontal- and vertical-plane images.

For far-field configurations, the clutter mean pixel power can also be evaluated analytically via the small perturbation method (SPM),[17] which is an approximate technique of calculating the mean RCS per unit area, or σ^0, for surfaces with small RMS height compared to the wavelength. Extensive numerical experiments have validated the accuracy of first-order SPM estimation of σ^0 against AFDTD computations, for a wide variety of sensing scenarios and parameters, including those considered in the current section.[18,19] For the rough surface models with exponential covariance function, the first-order SPM analytic expressions for σ^0 are, for the two polarization combinations, respectively[15,17]:

$$\sigma_{vv}^{0} = 2k_0^4 h_{RMS}^2 L_c^2 \sin^4\alpha \left| \frac{(\varepsilon_r - 1)\left(\varepsilon_r + (\varepsilon_r - 1)\cos^2\alpha\right)}{\left(\sqrt{(\varepsilon_r - \cos^2\alpha)} + \varepsilon_r \sin\alpha\right)^2} \right|^2 \left(1 + k_0^2 L_c^2 \cos^2\alpha\right)^{-\frac{3}{2}}, \tag{8a}$$

$$\sigma_{hh}^{0} = 2k_0^4 h_{RMS}^2 L_c^2 \sin^4\alpha \left| \frac{(\varepsilon_r - 1)}{\left(\sqrt{(\varepsilon_r - \cos^2\alpha)} + \sin\alpha\right)^2} \right|^2 \left(1 + k_0^2 L_c^2 \cos^2\alpha\right)^{-\frac{3}{2}}, \tag{8b}$$

where $k_0 = \frac{2\pi f}{c}$ is the free-space wavenumber at frequency *f*. To compute σ^0 over the wide frequency band characterizing the SAR images, we simply average the single-frequency values obtained from Eqs. 8a and 8b over that band. The mean pixel power is then given by $\sigma^0 A$, where A is the image resolution cell area (Note: the mean power per image pixel and the mean power per resolution cell are identical, regardless of the pixel size). This area is the product of the downrange and cross-range resolutions which, for far-field SAR images, has the expression

$$A = \frac{c^2}{4Bf_c\Delta\phi\cos\alpha}, \tag{9}$$

where f_c is the center frequency of the radar signal spectrum, and $\Delta\phi$ is the azimuth integration angle. The mean pixel power calculations based on Eqs. 8 and 9 are in excellent agreement (within fractions of 1 dB) with the numerical results obtained by AFDTD simulations. This fact makes us confident in applying the analytic formulas for clutter power estimation for a wide range of model parameters, as shown in the next section.

All the previous analytic clutter power estimations (including the formulas for σ^0 and A) assumed the image is created in the horizontal ground plane, as most side-looking SAR systems operate. If we consider an underground image in the vertical plane, the clutter mean pixel power is identical to that obtained in the horizontal plane, but σ^0 and A are not the same, due to differences in the downrange resolution between the two imaging modes, as shown by Eqs. 1a and 1b. Thus, the resolution cell area in vertical plane image shrinks by the factor $\tan\theta_2 = \frac{\cos\alpha}{\sqrt{\varepsilon_r - \cos^2\alpha}}$ as compared to the horizontal plane counterpart($A^V = A^H \tan\theta_2$), while the mean RCS per unit area increases by the factor $\frac{1}{\tan\theta_2} = \frac{\sqrt{\varepsilon_r - \cos^2\alpha}}{\cos\alpha}$ ($\sigma^{0V} = \sigma^{0H} / \tan\theta_2$; the superscripts V and H stand for vertical and horizontal plane images, respectively).

3.2 Target-to-Clutter Ratio

Before proceeding to estimate the TCR in the far-field, side-looking underground GPR images, we briefly discuss how to evaluate the target image power in these sensing scenarios. As with the near-field target signature in Section 2.2, we create the SAR images of a point target buried at various depths, for the same system parameters as those used in Section 3.1 for clutter evaluation. We assume that the target is in the image plane and perfectly focused. To calibrate the magnitude in these images, we use the image of a flush-buried M15 antitank landmine obtained in the same sensing scenario (45° depression angle). The variation of the point target image power with burial depth is displayed in Fig. 14a, together with the two-way attenuation curve as a function of the same depth. The latter is given by

$$Atten^{2-way} = \exp\left(-\frac{Z_0\sigma}{\sqrt{\varepsilon_r - \cos^2\alpha}} d\right). \tag{10}$$

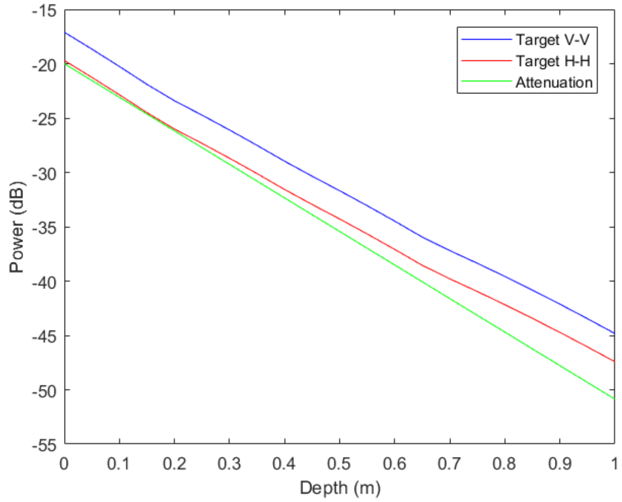

(a)

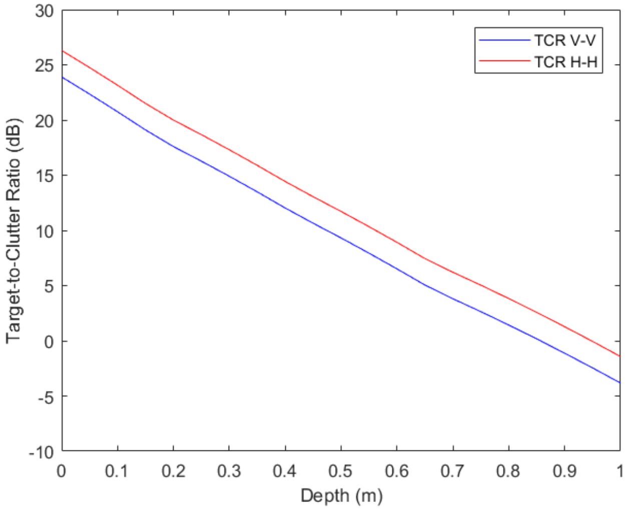

(b)

Fig. 14 Image power metrics as a function of depth for far-field side-looking underground images, showing: a) variation of the target image power as a function of burial depth; and b) variation of the TCR as a function of burial depth, in the presence of rough surface clutter

These graphs are very similar with those in Fig. 8 obtained for the near-field imaging geometry and reinforce the idea that the point target's image magnitude decrease with burial depth is largely dictated by the radar wave attenuation in the lossy ground medium. (Note: the fact that the absolute magnitude of the graphs in Figs. 8 and 14a are very close to one another is simply a coincidence, given that the near- and far-field images were created with different system parameters, image formation algorithms, and normalization factors). Since the mean clutter power is independent of depth for far-field images (as established in Section 3.1), the TCR follows the same variation as the target power (Fig. 14b). However, we notice that larger TCR is obtained in H-H than in V-V polarization due to the lower clutter power in the former case.

An interesting aspect of the target power calculation in far-field SAR images is that, when using the magnitude normalization in Eq. 5, the resolution cell containing the target has a power equal to its mean RCS when the average is computed over all frequencies and aspect angles involved in the imaging procedure. That allows the rapid evaluation of the target image power based directly on databases of RCS values, without going through the image formation process. For instance, in the imaging scenario considered in this section, for the flush-buried M15 landmine, we obtained a peak target image power of −18.1 dB for V-V polarization and −18.7 dB for H-H polarization. Evaluations of the mean RCS over the same sensing parameter space came out within 1 dB of these values. Importantly, to obtain a good match between the two sets of calculations, we must avoid any data windowing in the image formation procedure. The same method of evaluating the target image power based on the mean RCS is not available for near-field sensing scenarios, where the very concept of RCS is not well defined.

Another important investigation is the variation of the TCR with the radar incidence (depression) angle, with the purpose of finding the optimal operational geometry of the imaging system. To this end, we keep the point target at a fixed depth and vary the incidence angle, while assuming the target is included in the image plane. For a buried point target, the variation of its radar response with respect to the incidence angle follows that of the two-way transmission coefficient into and out of the ground. (As previously noted, this behavior may not necessarily be true for a real radar target, which may display its own intrinsic signature variation with the incidence angle). The expressions for these two-way transmission coefficients are as follows:

$$T_{vv}^{2-way} = \frac{4\varepsilon_r \sin\alpha \sqrt{\varepsilon_r - \cos^2\alpha}}{\left(\varepsilon_r \sin\alpha + \sqrt{\varepsilon_r - \cos^2\alpha}\right)^2}, \tag{11a}$$

$$T_{hh}^{2-way} = \frac{4\sin\alpha \sqrt{\varepsilon_r - \cos^2\alpha}}{\left(\sin\alpha + \sqrt{\varepsilon_r - \cos^2\alpha}\right)^2}. \tag{11b}$$

To estimate the clutter power, we use the analytic method outlined in Section 3.1, based on the direct computation of σ^0 and A. In our numerical model, we assume an imaging system with frequencies between 0.5 and 2 GHz, 60° integration angle (for all incidence angles), and a rough surface with h_{RMS} = 5 mm, L_c = 5 cm, and exponential covariance function. The target burial depth is d = 0.3 m. We use the graph in Fig. 14a to calibrate its image magnitude at 45° incidence: –26.0 dB for V-V polarization and –28.7 dB for H-H polarization.

The graphs characterizing the target power, the clutter power, and the TCR with respect to the incidence angle α are shown in Fig. 15. Note the similar angular variation of the target power and σ^0. In Fig. 15b, we also plotted the variation of the resolution cell area A with the incidence angle, given by Eq. 9. When represented in decibels, this variation is very small for incidence angles below 45° (the area difference between 0° and 45° is 1.5 dB), so the resolution cell area dependence on α has very little impact on the mean clutter power up to 45°. Consequently, the TCR displays relatively little variation for incidence angles below 45°, as seen in Fig. 15c. For these angles, the H-H polarization generates higher TCR than the V-V counterpart. Based on the angular dependence, we plotted the TCR as function of the radar–target ground range R_g, when the radar height is fixed (h = 5 m), in Fig. 15d. This graph shows a remarkably constant TCR for ranges exceeding the radar platform height.

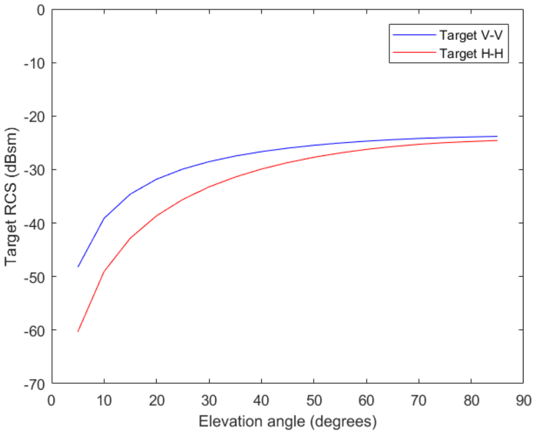

(a)

Fig. 15 Image power metrics as a function of incidence angle for far-field side-looking underground images, showing the variation of: a) the target image power with angle; b) the rough surface clutter σ^0 and resolution cell area with angle; c) TCR with angle; and d) TCR with ground range

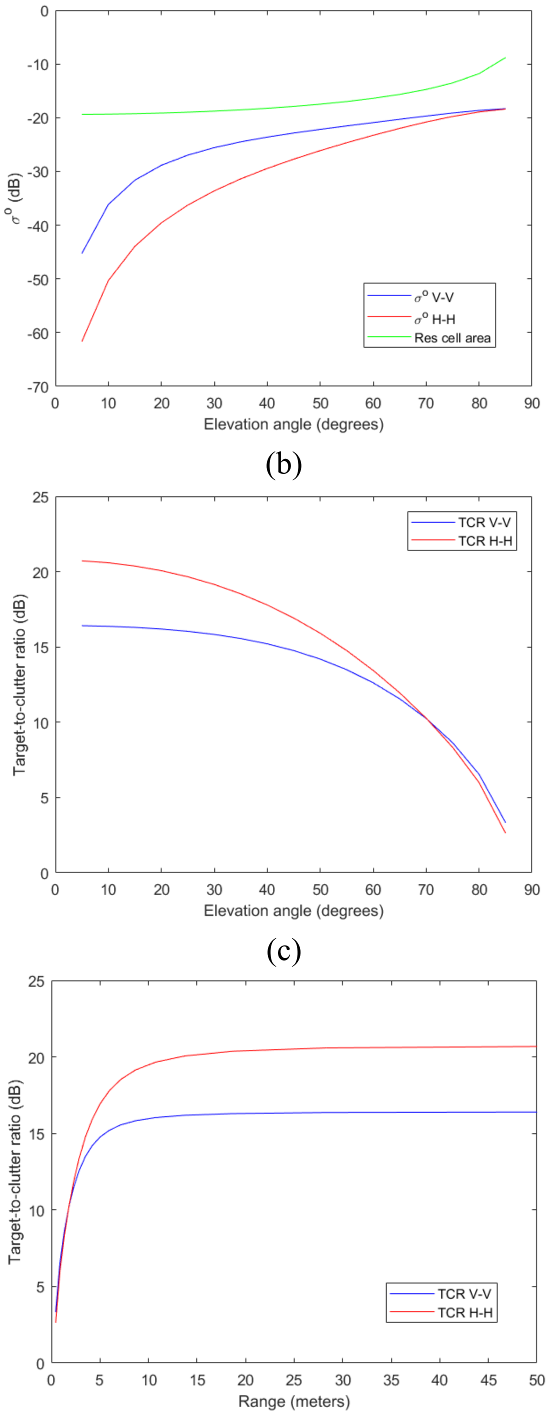

(b)

(c)

(d)

Fig. 15 Image power metrics as a function of incidence angle for far-field side-looking underground images, showing the variation of: a) the target image power with angle; b) the rough surface clutter σ^0 and resolution cell area with angle; c) TCR with angle; and d) TCR with ground range (continued)

Since most side-looking SAR imaging systems operate at depression angles between 20° and 45°, we can safely state that this angle choice has little impact on the TCR performance for buried targets in the presence of rough surface. When we repeated these simulations for various target burial depths up to 1 m we consistently arrived at the same conclusion. Another important observation is that the same TCR is obtained in both horizontal and vertical plane images, as long as the target is located in that image plane. For large incidence angles (60° or larger), the stretching of the resolution cell area starts to weigh more significantly on the clutter power and the TCR and we see a rapid drop in the latter. However, extrapolating these results to angles close to normal incidence ($\alpha = 90°$) does not make sense, since in that case we transition to the down-looking GPR SAR imaging system regime, where many of the assumptions used by the analysis in this report (particularly the far-field assumptions) become invalid.

3.3 Near-Field Image Analysis

After investigating some key phenomenological aspects of side-looking SAR imaging of buried targets in rough surface clutter in far-field configurations, we are ready to discuss the more realistic near-field imaging geometry encountered in UAV-based radar systems. The same elegant analytic formulations for estimating the target and clutter power presented for the far-field case are not available for near-field configurations. Therefore, it is more difficult to obtain general quantitative results in this case, given that each new sensing scenario would require a separate, time-consuming numerical EM model. Nevertheless, the simulations presented in this section allow us to point out some important qualitative differences between the near- and far-field modes and draw conclusions related to the SAR system's expected performance.

As shown in Section 3.2, the target image displays a very similar character between the near-field and far-field configurations, especially in terms of power variation with burial depth. However, when it comes to rough surface clutter in side-looking, near-field SAR images, we notice a strong variation of its mean power with downrange, due to changes in both radar-pixel range and angle of incidence (as a reminder, in far-field configurations, the mean clutter power was constant across the entire image extent). Consequently, we expect this effect to impact the TCR variation with target burial depth, for both horizontal and vertical plane images.

When looking at the TCR variation with the incidence angle, we do not anticipate significant differences between the near- and far-field cases, as long as the radar operates at long-enough ranges. As previously discussed, the term "long range" used in this report has a relative meaning; in practice, we found a 4-m-range from radar to the vertical imaging plane as enough to validate the subsequent analysis. In reference to Fig. 16, we call α_0 the incidence angle in the near-field geometry, $\alpha_0 = \operatorname{atan}\frac{h}{R_g}$. In the following, we keep the radar range $R_0 = \sqrt{h^2 + R_g^2}$ constant as we vary α_0. Then, a fixed target burial depth d will have to compete with the clutter projecting from the pixel at location P in the same figure. This pixel is seen by the radar at an angle

$$\alpha = \operatorname{atan}\frac{h}{R_g + d\frac{\sqrt{\varepsilon_r - \cos^2\alpha_0}}{\cos\alpha_0}}. \tag{12}$$

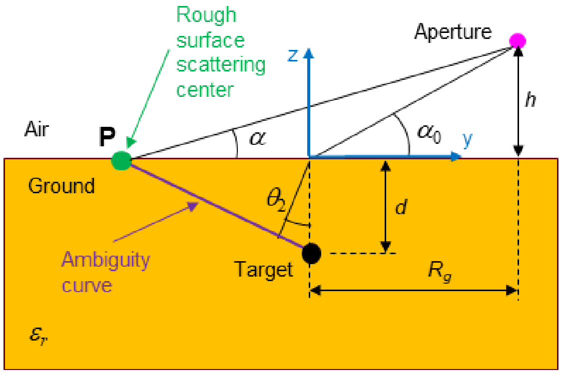

Fig. 16 Diagram illustrating the geometry of the side-looking imaging GPR system for near-field TCR calculations

The mean clutter power at the pixel P can be estimated by the same methods as in Section 3.1, using the incidence angle α. Moreover, for small target depths relative to the radar range R_0, α_0, and α are very close from one another. Consequently, we expect the variation of the clutter power and TCR with respect to the angle α_0 to conform to the plot in Fig. 15c, although with different absolute magnitudes. That is, the TCR has very little variation with that angle up to 45°, then drops rapidly due to the increase in the resolution cell area size. (Note: for near-field imaging in the ground plane, the resolution cell area is given by $A = \frac{c^2 R_0}{4Bf_c L_x \cos\alpha_0}$, where the aperture length L_x is assumed fixed). This statement holds as long as the ambiguity curves can be approximated by straight lines (as drawn in Fig. 16), which is the same as requiring a relatively long radar range, as discussed in the previous paragraph. Short-range sensing scenarios deviate from this theoretical analysis, as shown later in this section.

To investigate the TCR variation with target depth, we performed an AFDTD simulation of a near-field imaging scenario involving a rough surface with the same parameters as in Section 3.1. The frequency band extends from 0.5 to 2 GHz, the radar platform height is h = 1.6 m, the ground range to the image center is R_g = 3.8 m, and the aperture length is L_x = 7.6 m. Infinitesimal dipoles with the same orientation (along the z-axis for V-V polarization and along the x-axis for H-H polarization) were employed for both Tx and Rx. The target is buried at depths from 0 to 1 m, below the center of the ground-plane image at $x = 0$, $y = 0$. The ground has the same dielectric properties as in the previous sections. The imaging procedure included Hanning windows on the radar data in both frequency and aperture dimensions.

The resulting images obtained in the $z = 0$, $y = 0$, and $x = 0$ planes, for H-H polarization, are displayed in Fig. 17. From these images, it becomes clear that the mean clutter power decreases with increasing downrange, which represents the negative y direction in the horizontal-plane image in Fig. 17a and the negative z direction in the vertical-plane image in Fig. 17b. In reference to Fig. 16, we can establish a simple relationship between the y coordinate of a pixel in the horizontal-plane ($z = 0$) image and the depth d of its projection onto the vertical-plane ($y = 0$) image:

$$y = -\frac{d}{\tan\theta_2} = -d\,\frac{\sqrt{\varepsilon_r - \cos^2\alpha_0}}{\cos\alpha_0}. \qquad (13)$$

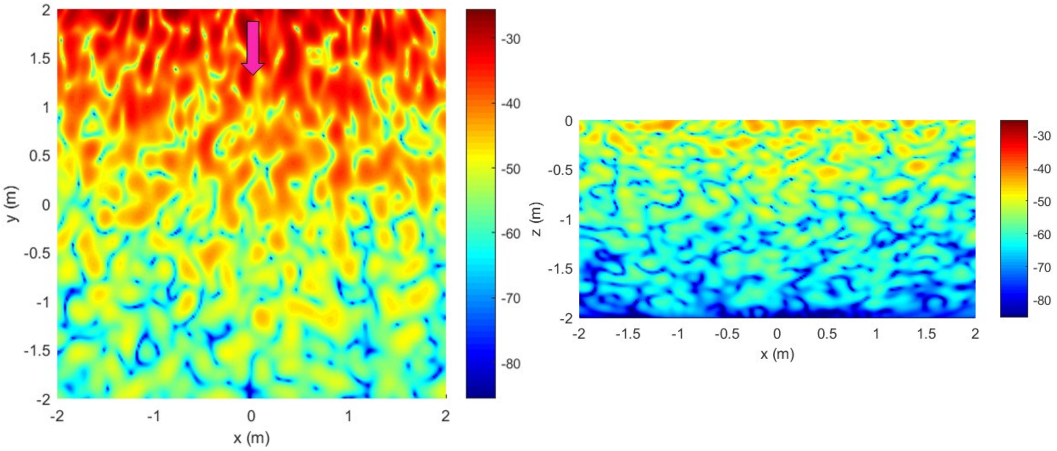

(a) (b)

Fig. 17 2-D images of rough surface clutter created by a near-field side-looking GPR system characterized by medium range and small incidence angle, in H-H polarization, shown in the following planes: a) $z = 0$; b) $y = 0$; and c) $x = 0$. The arrows indicate the radar look direction, or LOS.

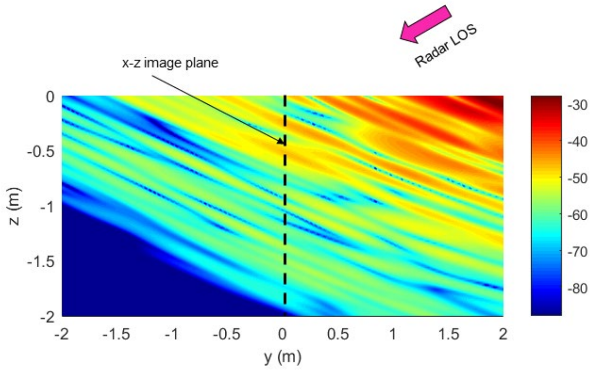

(c)

Fig. 17 2-D images of rough surface clutter created by a near-field side-looking GPR system characterized by medium range and small incidence angle, in H-H polarization, shown in the following planes: a) $z = 0$; b) $y = 0$; and c) $x = 0$. The arrows indicate the radar look direction, or LOS (continued).

The mean clutter power as a function of downrange ($R_g - y$) in the horizontal-plane image, and as a function of depth (negative z coordinate) in the vertical-plane image, is plotted in Fig. 18. The mean clutter power is computed as the average pixel power along lines of constant downrange (parallel to the x-axis). Since only a limited number of resolution cells are available for averaging along these lines, the graph displays significant oscillations around a trend line. On the same graphs, we plotted these trend lines by performing quadratic polynomial fits on the average pixel power data.

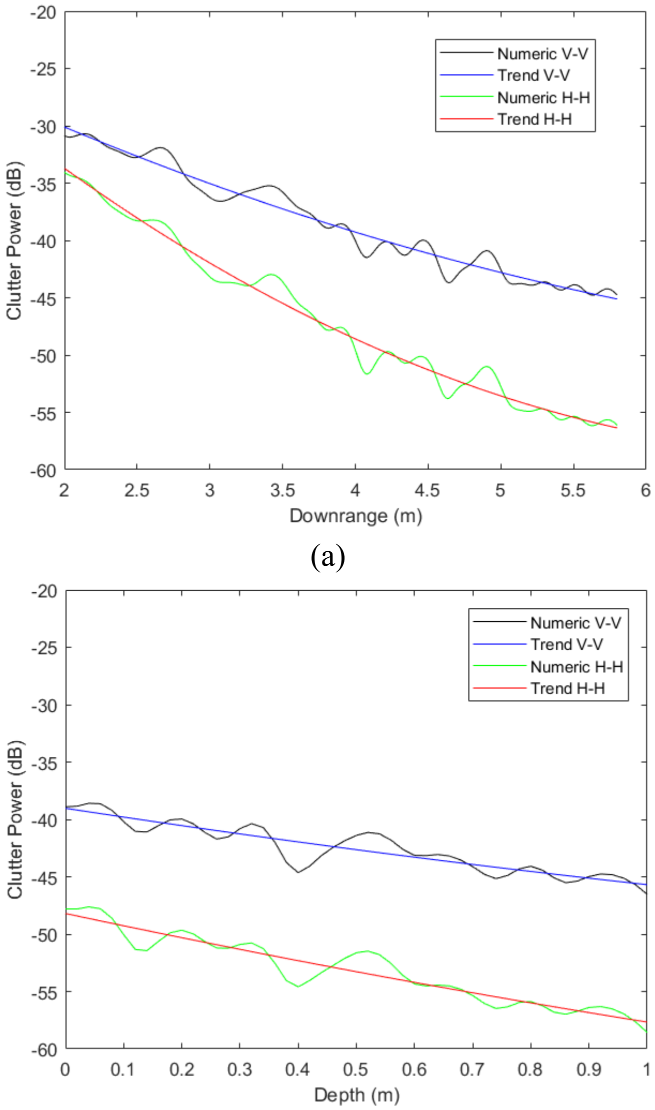

(a)

(b)

Fig. 18 Mean rough surface clutter power variation across 2-D images created by a near-field side-looking GPR system characterized by medium range and small incidence angle, showing: a) variation as a function of downrange (R_g-y) in the ground plane image; and b) variation as a function of depth (–z) in the vertical plane image

The graphs in Fig. 18b clearly show that the mean clutter power decreases with the image depth: the reduction at 1 m depth is about 10 dB for H-H polarization and 11 dB for V-V polarization. This is in contrast with the far-field case, where the mean clutter power was uniform across all images. As a reminder, the target image power as a function of depth, calibrated to the response of a flush-buried M15 landmine, was investigated in Section 2.2 and plotted in Fig. 8, for the same imaging system parameters as those used in this section. Putting all this information together, we obtain the TCR versus depth for this imaging system in Fig. 19. The graph indicates that, for this side-looking GPR SAR imaging scenario, the TCR decreases with increasing target burial depth, and that the H-H polarization offers better TCR (hence, better detection performance) than the V-V polarization.

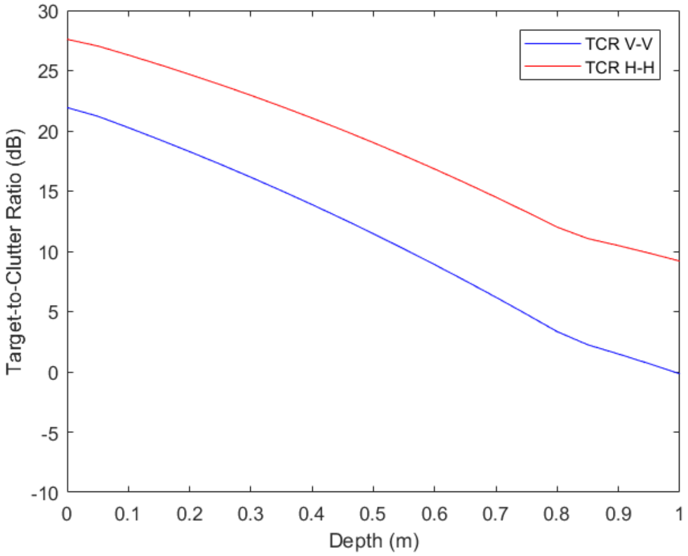

Fig. 19 TCR ratio as a function of depth for the 2-D images created by a near-field side-looking GPR system characterized by medium range and small incidence angle, in the presence of rough surface clutter

Not all near-field side-looking SAR geometries follow the same TCR variation with the target depth as in the previous example. That scenario was characterized by medium ground range and small incidence angle (α_0 = 23°), and consequently the ambiguity curves are approximately straight lines between the horizontal (ground) and vertical image planes (similarly to the PSF examples shown in Figs. 6 and 7). If we consider a sensing geometry involving short ground range and relatively large incidence angle, the ambiguity curves bend in a way that generates more rapid clutter power decay with increasing vertical-plane image depth. This scenario is closely associated with the PSF examples in Figs. 4 and 5.

To illustrate this point, we simulated the imaging of a rough surface with a near-range side-looking SAR system, characterized by platform height h = 1 m, ground range to image plane R_g = 1.2 m, and aperture length L_x = 7 m (all the other simulation parameters are identical to the previous model). The incidence angle from the middle of the aperture is α_0 = 40°. The simulation of this geometry was performed for H-H polarization only. The 2-D image in the x = 0 plane (shown in Fig. 20) is the most interesting one, since it shows the ambiguity curves obtained in that plane. Note the strong bending of these curves (as compared to those in Fig. 17c), combined with the rapid power decay at increasing range away from the radar, resulting in shallower clutter penetration of the underground space.

Consequently, we expect the mean clutter power to drop more rapidly with depth than in the scenario investigated in the previous simulation.

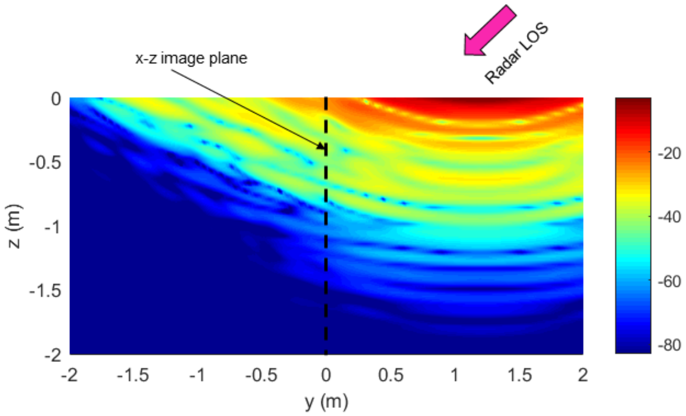

Fig. 20 **2-D image of rough surface clutter in the *x* = 0 plane, created by a near-field side-looking GPR system characterized by short range and medium incidence angle**

The variation of the target power, mean clutter power, and TCR with depth are shown in Fig. 21. The mean clutter power drops by about 25 dB at 1 m depth (compare that to the 10 dB drop in Fig. 18b). Since the target power drops by a similar amount with increasing depth, the resulting TCR is relatively constant. One could argue that the sensing geometry considered in this numerical example is somewhat contrived and does not describe the operational parameters of typical side-looking SAR systems. Instead, these systems normally operate at longer ranges and smaller incidence angles, hence the earlier example illustrated in Figs. 17–19 is more representative for this type of systems.

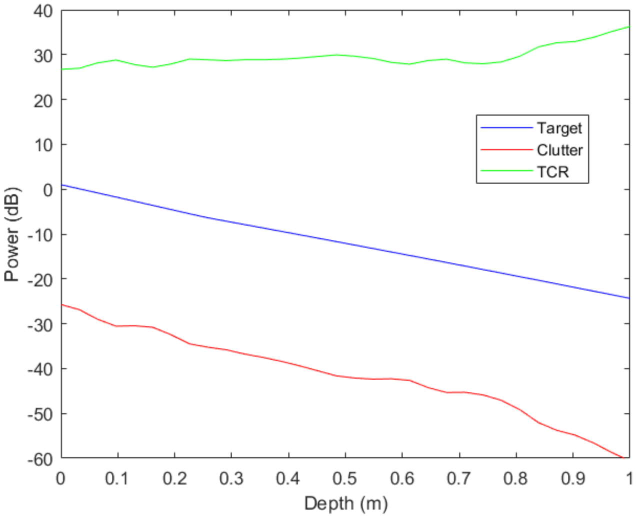

Fig. 21 **Target power, mean rough surface clutter power, and TCR as a function of depth for the 2-D images created by a near-field side-looking GPR system characterized by short range and medium incidence angle**

We can make further comparisons between the TCR performance of the side-looking GPR imaging systems considered in this report and that of a down-looking GPR imaging system investigated in our previous work.[4] The down-looking system involves a 7-m-long aperture placed at 1-m height, with all the other parameters identical to the side-looking cases. The 2-D image obtained in the $x = 0$ plane is shown in Fig. 22. In Fig. 23 we plotted the target power, mean clutter power, and TCR as a function of depth for the 2-D down-looking imaging system. The target power was calibrated to the response of a flush-buried M15 landmine, and the clutter was generated by a rough surface with parameters identical to those in this report. Only H-H polarization was considered for the down-looking GPR system.

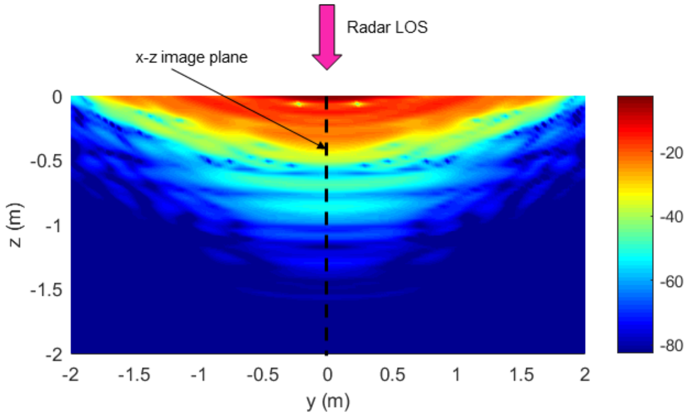

Fig. 22 2-D image of rough surface clutter in the $x = 0$ plane, created by a near-field down-looking GPR system

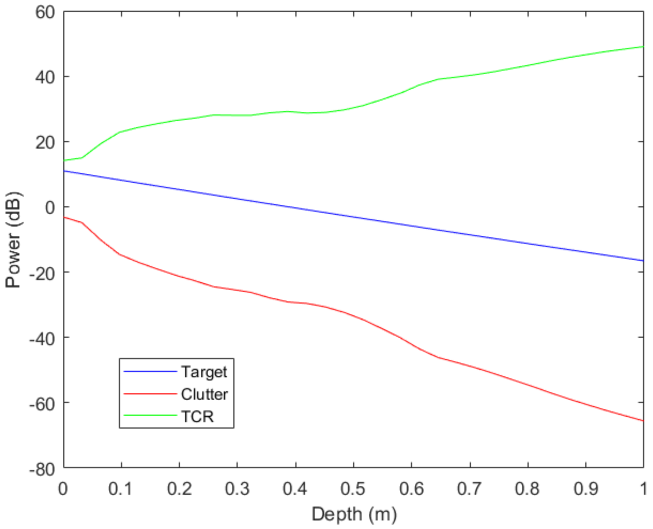

Fig. 23 Target power, mean rough surface clutter power, and TCR as a function of depth for the 2-D images created by a near-field down-looking GPR system

Fig. 24 summarizes these results by showing the TCR versus depth trend lines obtained in the down-looking case, together with the two side-looking scenarios investigated in this section. The interesting aspect to note is the opposite type of variation (increasing vs. decreasing TCR) between the graphs characterizing the down-looking and the first side-looking (medium range, small incidence angle) geometries. This difference comes primarily from the projection mechanism of the rough surface scattering centers onto the underground vertical-image plane, which was explained in Section 2. For down-looking systems, the clutter is strongly attenuated in depth due to the shallow geometry of the ambiguity curves, whereas for typical side-looking systems ("side-looking 1"), the clutter ambiguity curves extend deep under the surface, while incurring less attenuation than the target response as we move to larger depths. The second side-looking geometry (short range, medium incidence angle) is somewhere in between the other two: although we are still technically in the side-looking regime, the short ground range and medium incidence angle bring it closer to the down-looking geometry, as far as the clutter scattering center projection mechanism along the ambiguity curves.

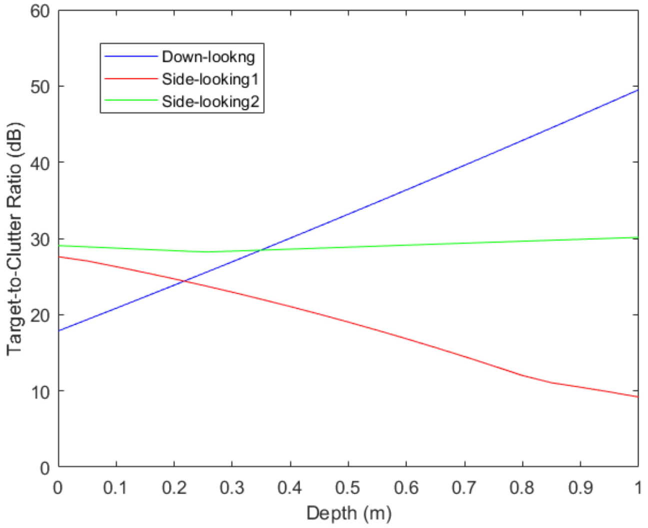

Fig. 24 TCR as a function of depth for the 2-D images created by a near-field GPR system in three different configurations, H-H polarization, in the presence of rough surface clutter. The side-looking 1 geometry is characterized by medium range and small incidence angle, whereas the side-looking 2 geometry is characterized by short range and medium incidence angle.

The important conclusion derived from this analysis is that the side-looking GPR sensing geometry may be appropriate for detecting shallow buried targets, whereas the down-looking GPR sensing geometry is clearly required in scenarios involving deep buried targets. For side-looking systems, the angle of incidence can be chosen anywhere between 20° and 45° with little penalty in performance. For those systems, horizontal- and vertical-plane images are equivalent in terms of TCR, as long as the image plane contains the target. For down-looking systems, a large improvement in TCR and detection performance can be achieved by upgrading from a 2-D to a 3-D imaging capability.[4]

4. Inhomogeneous Ground Clutter in Side-Looking GPR Imaging

Besides the rough ground surface, dielectric permittivity fluctuations in the underground propagation medium constitute another major clutter source in GPR sensing and imaging. A detailed study characterizing the inhomogeneous ground clutter in down-looking GPR imaging was performed in one of our previous reports.[4] Extrapolating those modeling scenarios to the side-looking GPR configuration has proved difficult, due to the increased computational load required to accommodate the side-looking geometries. Thus, we were unable to perform the simulation labeled "side-looking 1" in Fig. 24 (medium range, small incidence angle) in the presence of ground inhomogeneities. Therefore, we cannot generalize the conclusions derived from the simulations in this section to all possible side-looking GPR configurations. However, we think the results obtained in this section reveal some interesting effects that complement the rough surface clutter characterization from Section 3.

The soil dielectric permittivity fluctuations are modeled as a 3-D random process, with a specific covariance function (typically Gaussian or exponential), parametrized by the dielectric constant standard deviation and correlation length. The conductivity is modeled by a similar random process, perfectly correlated to the dielectric constant. Details related to this model's implementation in the AFDTD software can be found in a previous report.[4] For this study, we chose permittivity fluctuations with Gaussian covariance, mean values and standard deviations of $\overline{\varepsilon}_r = 5$ and $\sigma_\varepsilon = 0.8$ (for dielectric constant) and $\overline{s} = 0.02$ S/m and $\sigma_s = 0.003$ S/m (for conductivity), respectively. For the correlation length we selected two different values: $L_\varepsilon = 0.1$ m and $L_\varepsilon = 0.05$ m, with the note that the down-looking GPR study revealed a significant increase in underground clutter power when we transitioned from the former to the latter case.

In terms of sensing geometry, we compared the short-range side-looking configuration ($R_g = 1.2$ m) with the down-looking configuration. In both cases, the radar platform height is 1 m, the aperture length is 7 m, and the frequency band extends from 0.5 to 2 GHz. Only H-H polarization was considered in these simulations. The images in the vertical $y = 0$ plane obtained in the four cases (two different correlation lengths for down- and side-looking geometries) are shown in Fig. 25. As a general feature, the inhomogeneous clutter extends deeper in the vertical plane images than the rough surface counterpart: this is to be expected, since in the former case, physical scattering centers are located everywhere within the image plane (unlike the rough surface scattering centers, which are physically located only around the interface). Nevertheless, its mean power decreases with depth, primarily due to radar wave attenuation in the ground medium.

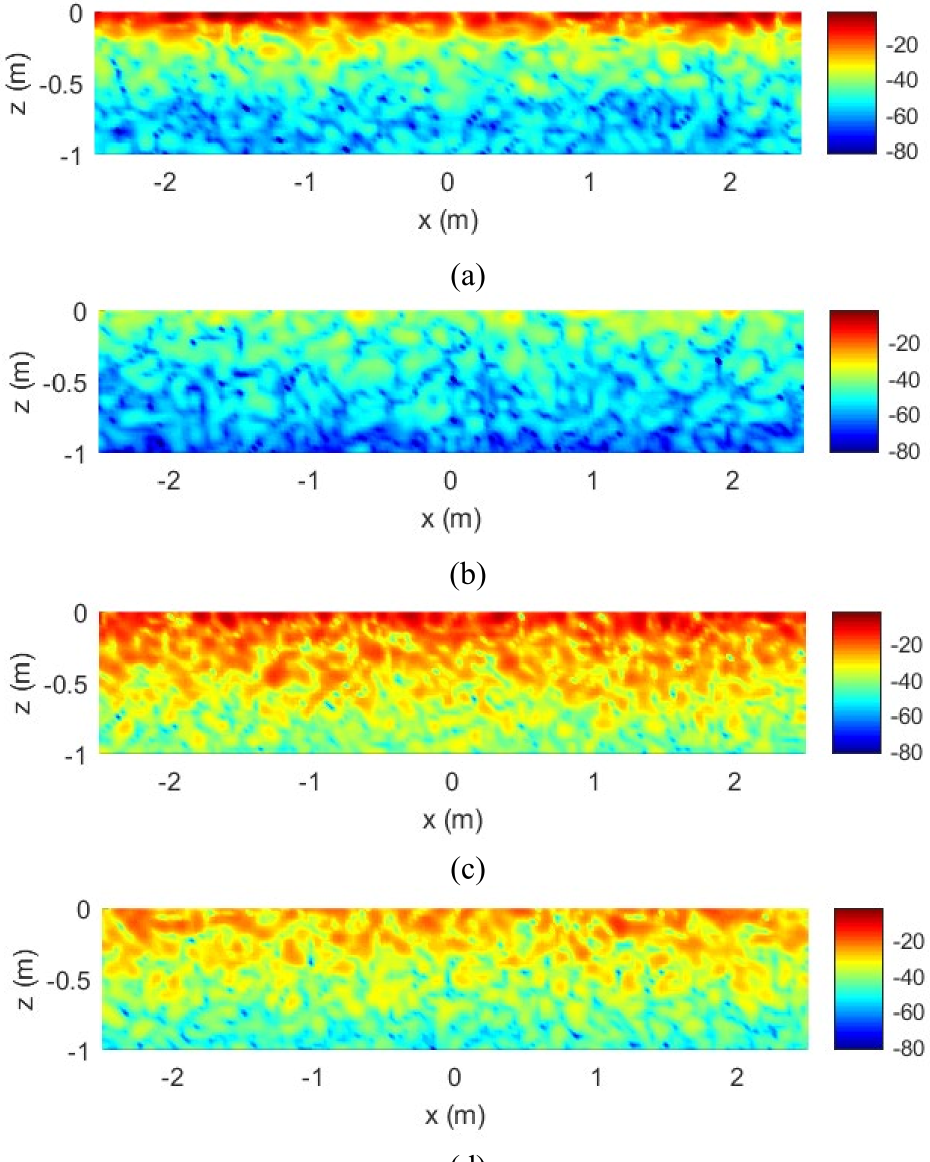

(a)

(b)

(c)

(d)

Fig. 25 2-D vertical plane ($y = 0$) images of clutter generated by inhomogeneous soil with dielectric constant mean of 5 and standard deviation $\sigma_\varepsilon = 0.8$, for the following cases: a) down-looking geometry with $L_\varepsilon = 0.1$ m; b) side-looking geometry with $L_\varepsilon = 0.1$ m; c) down-looking geometry with $L_\varepsilon = 0.05$ m; and d) side-looking geometry with $L_\varepsilon = 0.05$ m

Fig. 26 illustrates the target and clutter mean power as a function of burial depth, for the four cases investigated in Fig. 25. As in Section 3, the target power was calibrated to the response of a flush-buried M15 landmine. The TCR levels obtained in the same cases are shown in Fig. 27.

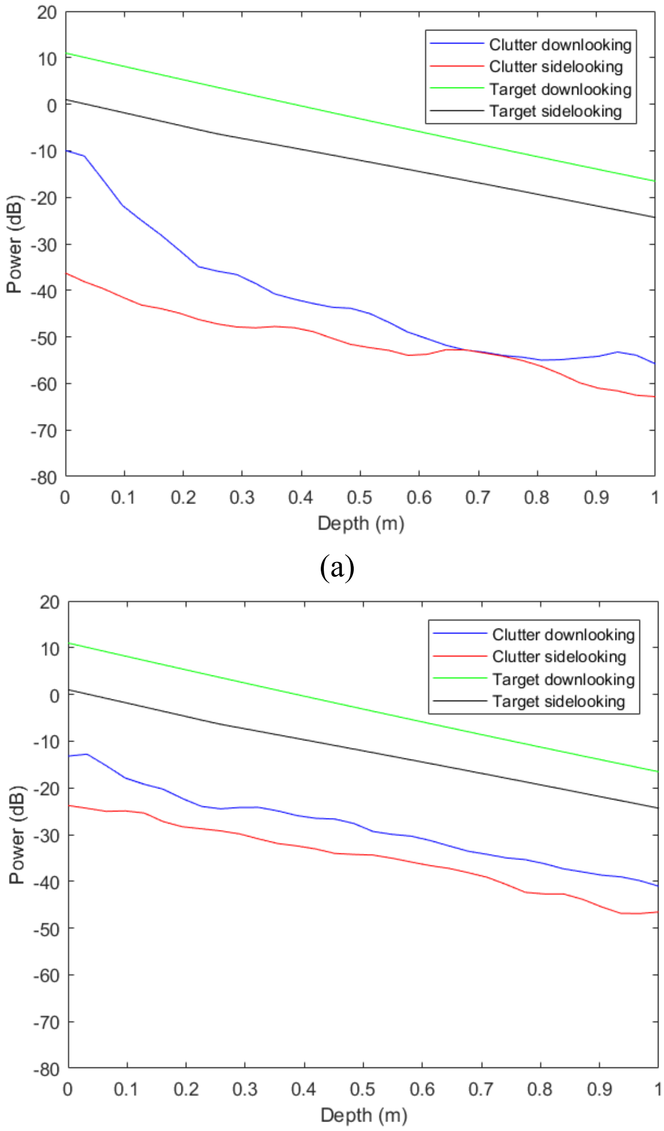

(a)

(b)

Fig. 26 Target and mean inhomogeneous-ground clutter power as a function of depth in the 2-D images created by down-looking and side-looking GPR systems, for two different correlation lengths of permittivity fluctuations: a) L_ε = 0.1 m; b) L_ε = 0.05 m

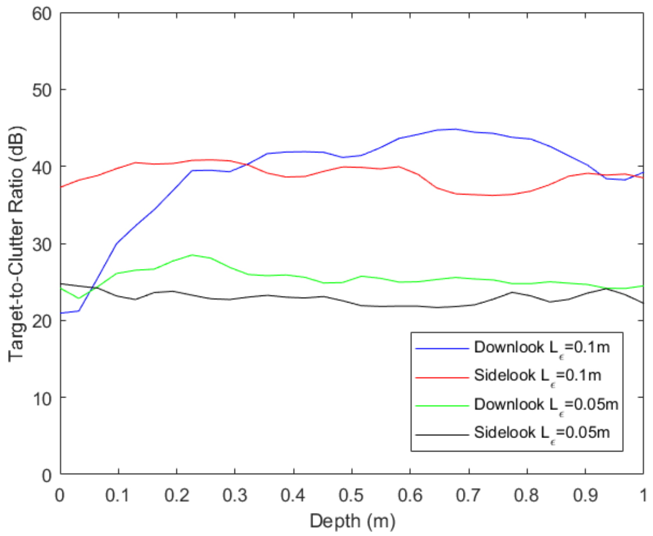

Fig. 27 TCR as a function of depth in the 2-D images created by down-looking and side-looking GPR systems in the presence of soil inhomogeneities, for two different correlation lengths of permittivity fluctuations and H-H polarization

The graphs in Fig. 27 suggest that, for the most part, the TCR is relatively constant with depth in the presence of inhomogeneous ground clutter. This can be explained by the fact that both target and clutter responses closely follow the wave attenuation curve, for both down-looking and side-looking sensing modes. The layers close to interface represent an exception in the down-looking case with large correlation length ($L_\varepsilon = 0.1$ m): the clutter in those layers is strong, but drops rapidly when the depth exceeds 0.2 m. This effect is due to the strong wave reflection at the transition from air to the inhomogeneous soil and was explained in more detail in our previous work.[4] (As a reminder, throughout this report, we always subtract the mean signal across the synthetic aperture from the radar data before proceeding with the image formation algorithm.) Interestingly, we do not notice the same rapid drop in clutter power in the side-looking configuration, since the direct reflection from the air–ground interface does not play a significant role in the radar signal in this case.

Combining the results in Figs. 24 (for rough surface clutter) and 27 (for inhomogeneous ground clutter), we reinforce the previous statement that, in general, the side-looking mode outperforms the down-looking counterpart at shallow target burial depths, but the down-looking mode offers better TCR at larger depths. In the down-looking case, we expect the inhomogeneous ground clutter to dominate the rough surface clutter at large depths; therefore, the TCR versus depth curve should flatten out (as in Fig. 27), rather than continue to grow (as in Fig. 24, which is probably unrealistic). However, in the typical side-looking geometry involving medium range, small incidence angle, the rough surface clutter projection is very strong at large depths and most likely dominates the inhomogeneous ground clutter; therefore, the TCR should keep decreasing with depth, as in the "side-looking 1" case in Fig. 24. In all these scenarios, when the clutter power becomes too low (e.g., at very large depths), the radar performance becomes limited by thermal noise or other interference sources rather than by clutter.

5. Conclusions

This report investigated the radar performance of side-looking GPR imaging systems via computer models. We considered sensing geometries compatible with an UWB radar installed on a low-flying UAV platform, which is characterized by short ranges. We assumed the system equipped with a single Tx-Rx channel, operating in SAR mode along a linear track and creating 2-D images of the underground space in various planes. The performance metric examined here was the TCR: this was obtained by creating the SAR images of a point target, as well as clutter, and taking the ratio of their mean powers. Both rough surface and inhomogeneous ground, which are the most prominent sources of distributed clutter relevant to GPR, were investigated in this work.

The modeling methodology was similar to that employed in one of our previous publications, where we focused our attention on down-looking GPR imaging systems.[4] Section 2 was mostly dedicated to investigating the PSF of side-looking GPR systems, with particular emphasis on out-of-plane imaging issues, including the ambiguity curves and surfaces, which received a detailed treatment. These issues are central to 2-D underground imaging systems, where we do not know a priori whether the target is included in the chosen image plane. When the target is physically located out of that plane, its projection on the 2-D image appears defocused and placed at the wrong coordinates. One possible mitigation strategy is to create 2-D images in multiple parallel planes and pick the one which displays the best-focused target.

Section 3 dealt with the clutter produced by rough ground surfaces in the underground images created by the side-looking GPR system. Although rough surface clutter is always present in conventional ground-plane images obtained from side-looking airborne SAR systems, it plays an outsized role in the underground images generated by the same systems, due to the out-of-image-plane projections of the scattering centers at the air–ground interface. These projections incur little attenuation with depth in the ground medium and end up competing with the target response, which in turn is strongly attenuated due to the propagation losses in the same medium.

Several GPR imaging simulation scenarios involving rough surface clutter were considered in Section 3, including far-field and near-field configurations. The analysis showed that similar TCR numbers are obtained in horizontal and vertical image planes as a function of target burial depth, as long as the target is included in the image plane. At the same time, H-H polarization offers better performance than the V-V counterpart, due to the reduced amount of clutter in the former case. For long-enough ranges, the TCR has little variation with the incidence angle when it is kept below 45°. For larger incidence angles, the TCR drops rapidly due to the resolution cell area stretching in the horizontal plane; however, the far-field assumptions underpinning this analysis tend to break down in this regime.

The TCR of GPR systems in the presence of rough surface clutter generally goes down with increasing target burial depth, for typical side-looking geometries involving medium ranges and small incidence angles. When we simulated a short-range, medium incidence angle system, we found out that the TCR versus depth curve flattens out. Moreover, when we transition to a down-looking GPR system, the TCR trends up with the target depth. These effects were explained by the differences in ambiguity curve geometries between the various radar sensing configurations.

In Section 4, we examined the clutter generated by permittivity fluctuations in the ground medium. Certain limitations of the computational models restricted our analysis to short-range side-looking GPR systems in this case. Nevertheless, the simulations consistently yielded relatively flat TCR versus depth curves for side-looking GPR configurations. This is indicative of the fact that both target and clutter power closely follow the variation of the radar wave attenuation with depth.

Before drawing overall conclusions from this study, as well as our preceding investigations into GPR imaging systems, we first need to recognize the limited number of scenarios we have been able to simulate in support of our analysis. Thus, to avoid the public release of the radar signature of specific, sensitive IED targets, we based most of the investigation on point targets, calibrated in magnitude to the response of buried generic landmines. In terms of radar clutter, we used statistical model parameters available in the open literature; these parameter sets may only be representative for certain terrain types and geographical locations, so we cannot make any generality claim about our clutter models. Additionally, other sources of noise, interference, and/or clutter may have important performance-limiting effects on the GPR system. As a consequence, the expected performance figures obtained in these reports cannot be construed as definitive proof of whether the radar system "works" or "does not work" on specific targets and environments. Instead, our primary purpose has been to derive general trends in radar performance as a function of various engineering and operational parameters, with the further goal of helping the system designer develop a more effective radar sensor for this application.

The down-looking GPR imaging mode offers the best performance for most buried target emplacements except for very shallow ones. As demonstrated in a previous study, a 3-D down-looking GPR imaging system vastly outperforms the 2-D version of the same, although it typically involves a larger, heavier and more expensive built. The TCR versus depth characteristic of this mode is relatively modest in a layer close to the air–ground interface, but displays a significant jump up at larger depth (this depth varies depending on whether we deal with a 2-D or 3-D imaging system, but can be evaluated at around 0.1–0.2 m). Eventually, the TCR curve becomes flat at ever larger depths, where the inhomogeneous ground clutter dominates the rough surface clutter.

The side-looking GPR mode, which involves 2-D imaging configurations, could be useful in detection of shallow-buried targets, but its performance degrades rapidly at larger target burial depths. The images can be created in either horizontal or vertical planes: the TCR is largely equivalent between the two. The key requirement to ensure proper target focusing is to choose an imaging plane that includes the target location. When this condition is satisfied, the incidence angle does not have a large impact on the TCR as long as it is no larger than 45°. H-H polarization offers better TCR than the V-V polarization; however, the V-V polarization may also be useful in side-looking GPR imaging systems in cases where it reveals particular target signature features not available in other modes.

One should add that the disturbed soil around the target burial site can sometime produce a sizeable signature detectable in the ground-plane image generated by a side-looking SAR system. This can be a useful indication of the target presence, even though the target's signature is too weak to make a direct impact in the radar image. Moreover, the side-looking SAR mode with imaging in the ground plane is the preferred sensing configuration for on-surface targets in CEH applications. For these reasons, this sensing modality will always have a firm place in these applications. As a topic of future research, we can also envision a combination of side-looking and down-looking SAR systems working cooperatively in a distributed radar network.

6. References

1. Dogaru T. Imaging study for small-UAV-mounted ground penetrating radar: Part I – Methodology and analytic formulation. CCDC Army Research Laboratory (US); 2019 Mar. Report No.: ARL-TR-8654.
2. Dogaru T. Imaging study for small-UAV-mounted ground penetrating radar: Part II – Numeric examples and performance analysis. CCDC Army Research Laboratory (US); 2019 June Report No.: ARL-TR-8725.
3. Dogaru T. Imaging study for small-UAV-mounted ground penetrating radar: Part III – A multi-static approach. CCDC Army Research Laboratory (US); 2019 Mar. Report No.: ARL-TR-8654.
4. Dogaru T. Clutter characterization for down-looking ground penetrating radar imaging. DEVCOM Army Research Laboratory (US); 2021 Oct. Report No.: ARL-TR-9327.
5. Richards M, Scheer J, Holm W. Principles of modern radar – basic principles. SciTech Publishing; 2010.
6. Dogaru T, Le C. Polarization differences in airborne ground penetrating radar performance for landmine detection. Proceedings of SPIE. 2016;9829.
7. Nguyen L, Ranney K, Sherbondy K, Sullivan A. Detection of buried in-road IED targets using airborne ultra-wideband (UWB) low-frequency SAR. Proceedings of the 60th MSS Tri-Service Radar Symposium; 2014.
8. Hubbard W, Bishop G, Gagnon J-P, Lagueux P, Hannuna S, Campbell N. Detection of disturbed earth using hyperspectral LWIR imaging data. Proceedings of SPIE. 2010;7835.
9. Liao D. Electromagnetic investigation on imaging of disturbed earth feature for buried target detection. Proceedings of SPIE. 2012;8361.
10. Dogaru T, Le C, Sullivan A. Disturbed earth effects in airborne radar detection of inroad threats. Proceedings of the 62nd Annual MSS Tri-Service Radar Symposium; 2016.
11. Balanis C. Advanced engineering electromagnetics. Wiley; 1989.
12. Dogaru T. AFDTD user's manual. Army Research Laboratory (US); 2010 Mar. Report No.: ARL-TR-5145.
13. Dogaru T. NAFDTD – a near-field finite difference time domain solver. Army Research Laboratory (US); 2012 Sep. Report No.: ARL-TR-6110.

14. Department of Defense High Performance Computing Modernization Program web page [accessed 2021 Dec]. https://centers.hpc.mil/.

15. Ulaby FT, Long DG. Microwave radar and radiometric remote sensing. University of Michigan Press; 2014.

16. Tsang L, Kong J, Ding K. Scattering of electromagnetic waves: theories and applications. Wiley; 2000.

17. Tsang L, Kong J. Scattering of electromagnetic waves: advanced topics. Wiley; 2001.

18. Liao D, Dogaru T. Full-wave characterization of rough terrain surface scattering for forward-looking radar applications. IEEE Transactions on Antennas and Propagation. 2012;60(8):3853–3866.

19. Dogaru T, Liao D. Validating models of bistatic scattering from dielectric surfaces with small roughness. Proceedings of the IEEE Antennas and Propagation Symposium; 2018.

Appendix. Analytic Description of the Ambiguity Curves and Surfaces in Ground Penetration Radar Imaging

In this Appendix we investigate the equations governing the ambiguity curves and surfaces present in images created with a ground penetrating radar (GPR) system operating along a linear synthetic aperture track along the *x* direction. A diagram of the geometry involved in these calculations is presented in Fig. A-1. The target coordinates are (x_0, y_0, z_0), while the radar coordinates are (x_r, y_r, z_r) (note that we replaced R_g by y_r and h by z_r). The formulation established here is valid for both down- and side-looking configurations.

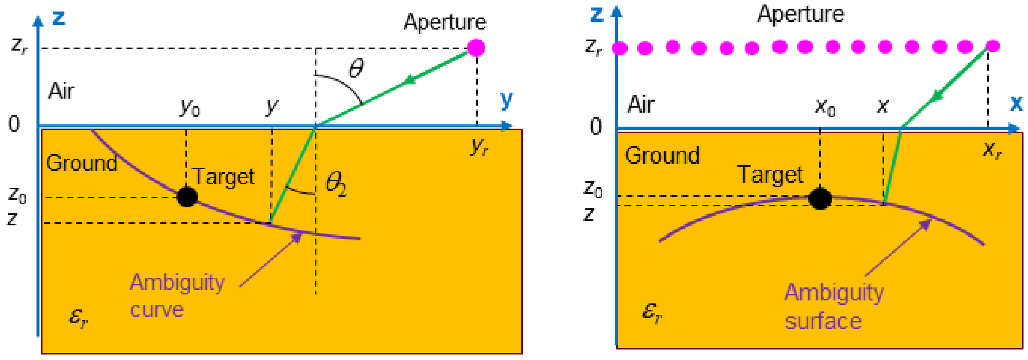

(a) (b)

Fig. A-1 Diagrams showing the geometry relevant to the ambiguity curves and surfaces in the a) y-z plane; b) x-z plane

The ambiguity curves were illustrated in multiple GPR images throughout the main report: they intuitively represent the image traces created in a plane orthogonal to the aperture by the target response. More exactly, we define the ambiguity curve as the locus of the points in that plane characterized by the same propagation path length from the radar location as the true target position.

When we consider the 3-D image trace created by the same target response, we notice that, in underground images, a certain amount of defocusing occurs, which causes this trace to extend farther in the cross-range (or *x*) direction. In that case, we talk about the ambiguity surface, which goes through the middle of the target trace obtained in the 3-D space. The purpose of this Appendix is to establish the equations describing the ambiguity curves and surfaces generated by a point target with arbitrary position in the underground region.

We start by showing the complete image of a point target placed at the air–ground interface at coordinates $(0,-2,0)$ m, in the entire $x = 0$ plane, which is perpendicular to the aperture (placed at $z_r = 1$ m, $y_r = 0$) and contains the target, in Fig. A-2. The radar frequencies and ground dielectric properties are the same as in the other numerical examples throughout this report. As obvious from the radar sensing geometry, in the upper half-space ($z > 0$), the ambiguity curves are circles centered at the aperture $\left(y_r, z_r\right)$ coordinates and going through the target location. The trace left by this response in the 3-D upper half-space has the shape of a circular “tube” with a uniform cross section. This uniformity follows from the symmetry of the sensing geometry, is specific to the free-space propagation case, and implies that no defocusing occurs in imaging planes located away from the target position.

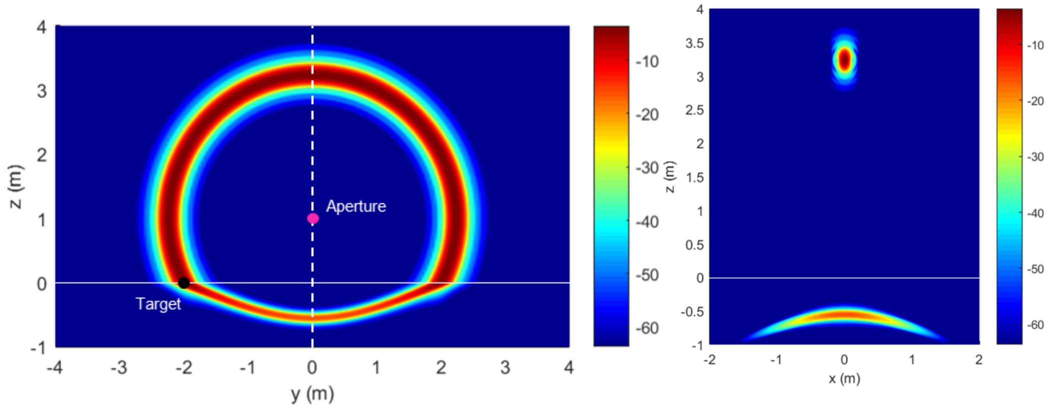

(a) (b)

Fig. A-2 Images of a point target obtained with a GPR system involving a linear synthetic aperture in the x direction, obtained in a) the x = 0 plane; b) the y = 0 plane

The situation is different when we consider the target image trace in the lower half-space ($z < 0$). As demonstrated throughout the main report, when the underground imaging plane does not include the target, the target’s image appears smeared in the cross-range direction, indicating some degree of defocusing. Therefore, this effect is specific to radar underground imaging in a half-space (air–ground) environment and does not have an equivalent in conventional free-space radar imaging (which includes ground–plane imaging as the most frequently used configuration). The difference between the two cases is clearly on display in Fig. A-2b, showing the image in the $y = 0$ plane, which does not contain the target: the aboveground image (around $z = 3.2$ m) appears correctly focused, whereas the underground image (around $z = –0.5$ m) is defocused.

To find the general equation of the ambiguity curve, we consider the sensing geometry depicted in Fig. A-1a, in the $x = x_0$ plane, where $\left(x_0, y_0, z_0\right)$ are the target coordinates, with the radar positioned in the same plane (i.e., $x_r = x_0$). We describe the ambiguity curve by two parametric equations $y = f_1\left(\theta\right)$ and $z = f_2\left(\theta\right)$, using the angle θ as free parameter. The following equations can be established:

$$\frac{z_r}{\cos\theta} - \frac{z}{\cos\theta_2}\sqrt{\varepsilon_r} = R, \tag{A-1a}$$

$$\left|y_r - y\right| = z_r \tan\theta - z \tan\theta_2, \tag{A-1b}$$

$$\sin\theta = \sqrt{\varepsilon_r}\,\sin\theta_2. \tag{A-1c}$$

In Eq. A-1a, R represents the propagation path length between the radar and target: this is the sum of propagation distances above and below the air–ground interface, the latter adjusted by the $\sqrt{\varepsilon_r}$ factor. As discussed elsewhere,[1] R cannot be computed in closed form for arbitrary target positions under the ground plane—a numeric procedure is required for this calculation. If the target is located in the ground plane ($z_0 = 0$), then we have $R = \sqrt{\left(y_r - y_0\right)^2 + z_r^2}$. Equation A-1c represents Snell's law and is used to eliminate θ_2 from the system of equations. The loss tangent[2] of the ground medium is assumed small (less than 0.1), such that we can keep only the real part of the dielectric constant ε_r. Another observation is that, in this system of equations, we always take $z \le 0$. Solving for y and z we obtain the following parametric equations:

$$y = y_r \pm \left(z_r \tan\theta \frac{\varepsilon_r - 1}{\varepsilon_r} + R \frac{\sin\theta}{\varepsilon_r} \right), \tag{A-2a}$$

$$z = \frac{\sqrt{\varepsilon_r - \sin^2\theta}}{\varepsilon_r} \left(\frac{z_r}{\cos\theta} - R \right). \tag{A-2b}$$

The range of variation for the parameter θ is taken such that we enforce the $z \le 0$ condition. Alternatively, we can formulate the ambiguity curve equation as $z = f\left(y\right)$ by using y as a free parameter, numerically solving the nonlinear Eq. A-2a in the variable θ (as a function of y), then plugging that solution into Eq. A-2b. Numerical experiments show very good overlap between the curves obtained via Eq. A-2 and the point target images. Two examples are shown in Fig. A-3, with the target at $\left(0,-2,0\right)$ m. In Fig. A-3a, the 8-m-long aperture is placed at $z_r = 1$ m, $y_r = 1$ m, whereas in Fig. A-3b, the aperture is placed at $z_r = 5$ m, $y_r = 10$ m.

---

[1] Dogaru T. Imaging study for small-UAV-mounted ground penetrating radar: Part I – Methodology and analytic formulation. CCDC Army Research Laboratory (US); 2019 Mar. Report No.: ARL-TR-8654.

[2] Balanis C. Advanced engineering electromagnetics. Wiley; 1989.

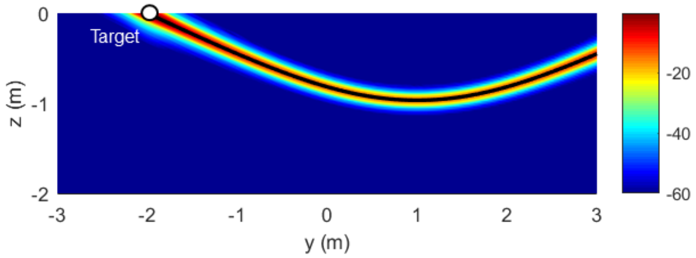

(a)

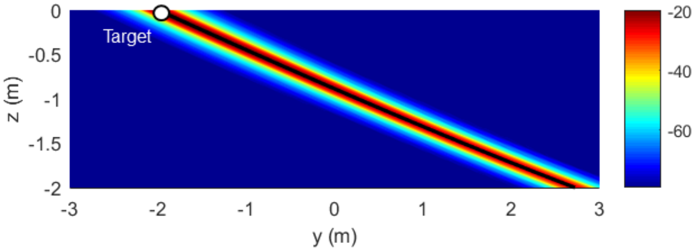

(b)

Fig. A-3 Images of a point target placed at coordinates (0,–2,0), obtained with a synthetic aperture located at a) z_r = 1 m, y_r = 1 m; b) z_r = 5 m, y_r = 10 m. The overlapping black lines are the ambiguity curves obtained from Eq. A-2.

The major limitation of the analysis so far is that it only considers the image in the $x = x_0$ plane and, additionally, it only takes into account the radar signal obtained at the aperture sample located at $x_r = x_0$. To obtain the ambiguity surface in the entire 3-D space, we need to account for the coherent summation of the radar signals at all spatial samples along the synthetic aperture, performed by the imaging algorithm. Two graphic representations of the ambiguity surface are shown in Fig. A-4. Fig. A-4a was obtained for a point target placed at $\left(0,-3,0\right)$ m, while Fig. A-4b is for a point target placed at $\left(0,-2,-1\right)$ m, with an 8-m-long radar aperture located at z_r = 1 m, y_r = 0.

We notice that the ambiguity surface has a saddle-like shape with minimum width (in the *x* direction) at the target location. This location has a mirror image with respect to the synthetic aperture position. The surface becomes wider in the *x* direction (indicative of image defocusing) as we move away from the target location. Another empirical fact we noticed in the GPR simulations is that increasing the integration angle increases the amount of defocusing as well. The ambiguity surface is not as well delimited in the 3-D space as the graphics in Fig. A-4 suggest. In reality, the image magnitude exhibits a gradual fading in the *x* direction, emanating from its center located along the ambiguity curve. The graphics in Fig. A-4 actually represent isosurfaces with magnitude –50 dB with respect to the brightest voxel, taken through the 3-D radar images.

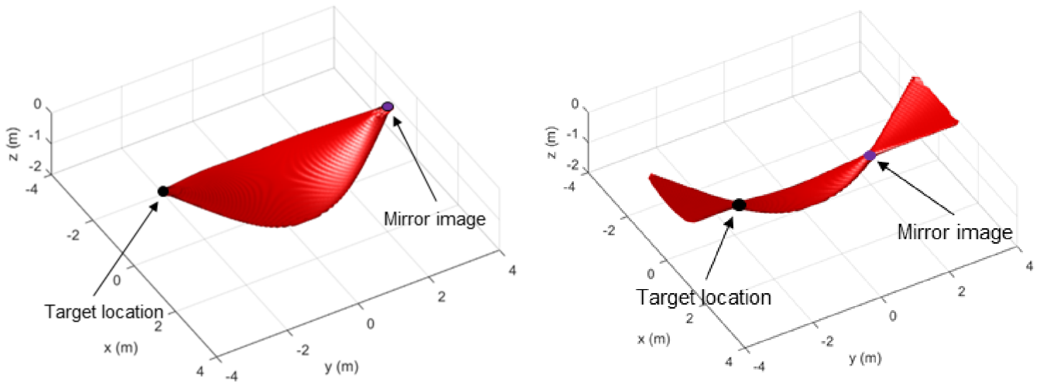

(a) (b)

Fig. A-4 Ambiguity surfaces obtained with the side-looking GPR imaging system, for point targets placed at a) (0,–3,0) m, b) (0,–2,–1) m

To derive the equations governing the ambiguity surface we develop the following ad hoc procedure: we assemble this surface from ambiguity curves obtained in vertical planes that go through the radar position along the synthetic aperture and the target position (these are the *u-z* planes in Fig. A-5). In each of these planes, the ambiguity curve is computed by the procedure summarized in Eq. A-2. As we move the radar position along the aperture, the collection of ambiguity curves thus generated define a surface in the 3-D space: this is the ambiguity surface. Although we cannot offer a rigorous justification for this procedure, the match with the imaging simulation results is very good in practice.

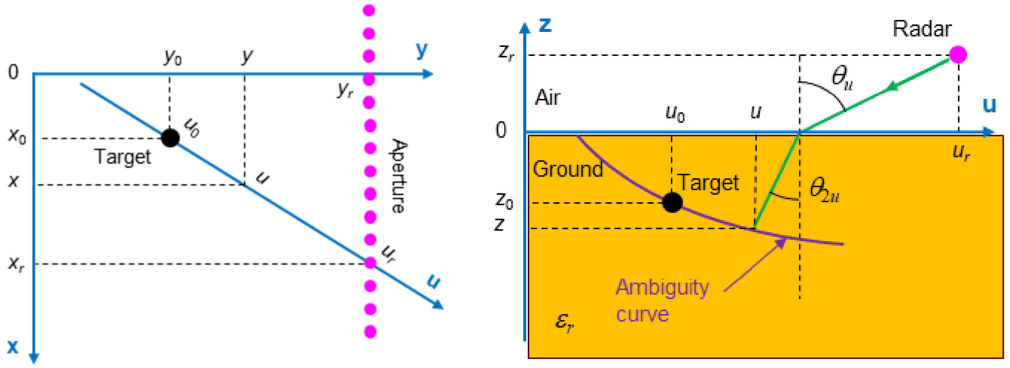

(a) (b)

Fig. A-5 Diagrams showing the geometry used in the ambiguity surface derivation in the a) x-y plane (top view); b) u-z plane

Let u_0 and u_r be the coordinates of the target and radar, respectively, along the rotated *u* axis, as in Fig. A-5, and *u* the coordinate of the current point on the ambiguity surface. In the *u-z* plane, which contains both the radar and target locations, we can write the following equations (similar to Eq. A-2):

$$\left|u_r - u\right| = z_r \tan\theta_u \frac{\varepsilon_r - 1}{\varepsilon_r} + R\frac{\sin\theta_u}{\varepsilon_r}, \tag{A3a}$$

$$z = \frac{\sqrt{\varepsilon_r - \sin^2\theta_u}}{\varepsilon_r}\left(\frac{z_r}{\cos\theta_u} - R\right), \tag{A3b}$$

where R is again the radar–target propagation path length. As previously discussed, R cannot be found analytically for arbitrary target locations but must be computed numerically. If the target is located in the ground plane, then we have $R = \sqrt{\left(x_r - x_0\right)^2 + \left(y_r - y_0\right)^2 + z_r^2}$. Additionally, we have

$$u_r - u = \left(u_r - u_0\right)\frac{y_r - y}{y_r - y_0}, \tag{A-4a}$$

$$\left|u_r - u_0\right| = \sqrt{\left(x_r - x_0\right)^2 + \left(y_r - y_0\right)^2}, \tag{A-4b}$$

$$x - x_0 = \left(x_r - x_0\right)\frac{y - y_0}{y_r - y_0}. \tag{A-4c}$$

Eliminating u, u_0, and u_r from these equations we obtain

$$y = y_r \pm \left[1 + \left(\frac{x_r - x_0}{y_r - y_0}\right)^2\right]^{-\frac{1}{2}}\left(z_r \tan\theta_u \frac{\varepsilon_r - 1}{\varepsilon_r} + R\frac{\sin\theta_u}{\varepsilon_r}\right), \tag{A-5a}$$

$$z = \frac{\sqrt{\varepsilon_r - \sin^2\theta_u}}{\varepsilon_r}\left(\frac{z_r}{\cos\theta_u} - R\right), \tag{A-5b}$$

$$x = x_0 + \left(x_r - x_0\right)\frac{y - y_0}{y_r - y_0}. \tag{A-5c}$$

Ordinarily, we can define a surface in the 3-D space by expressing the coordinates x, y, and z as functions of two free parameters. We can choose x_r as one of these free parameters. However, θ_u cannot be taken as a free parameter because it depends on x_r (or the direction of the u axis). Instead, we pick y as the second free parameter. Subsequently, we solve the nonlinear Eq. A-5a in θ_u, as a function of x_r and y, and then plug this solution into Eq. A-5b to find z. Finally, Eq. A-5c yields the coordinate x of the ambiguity surface.

To demonstrate the accuracy of these calculations, we present cuts through the ambiguity surface in constant-y-plane images, in Fig. A-6. For the numerical example in Fig. A-6a, we placed two point targets at coordinates $\left(0,-3,0\right)$ m and

$(0,-1.5,0)$ m, respectively, with the aperture at $z_r = 1$ m, $y_r = 0$, and created the image in the $y = 1$ m plane. In Fig. A-6b we considered two point targets at coordinates $(2,-3,0)$ m and $(2,-1.5,0)$ m, with the aperture at $z_r = 1$ m, $y_r = 0$, and created the image in the $y = 1$ m plane. In both cases, the aperture is 8-m-long and centered at $x = 0$. Since the targets are placed symmetrically with respect to the aperture in Fig. A-6a (x_0 is the same as the aperture center), the ambiguity surface is also symmetric. That is not the case in Fig. A-6b, where the targets are placed at an offset with respect to the aperture center. In both cases, the match between the simulated image data and the calculations based on Eq. A-5 is very good.

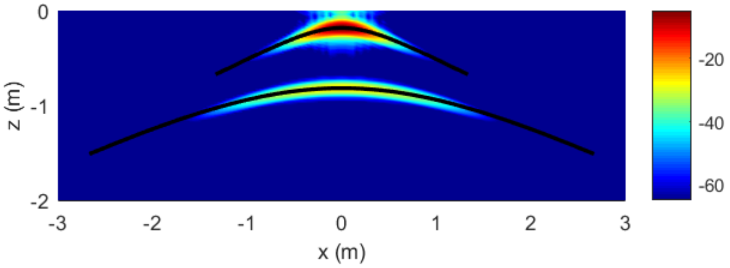

(a)

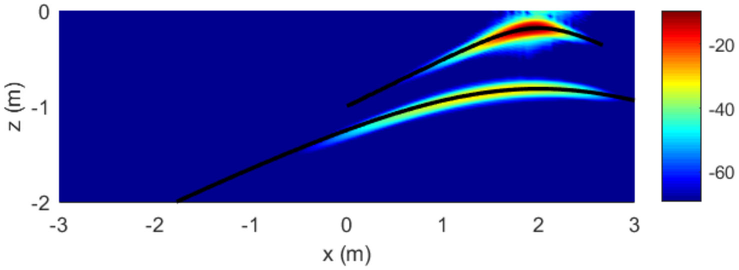

(b)

Fig. A-6 Images of two point targets, obtained in the y = 1 m plane, with a synthetic aperture located at $z_r = 1$ m, $y_r = 0$ m, for the following target coordinates: a) (0,–3,0) m and (0,–1.5,0) m; b) (2,–3,0) m and (2,–1.5,0) m. The overlapping black lines are cuts through the ambiguity surfaces obtained from Eq. A-5.

List of Symbols, Abbreviations, and Acronyms

2-D	one-dimensional
3-D	two-dimensional
ARL	Army Research Laboratory
CEH	counter-explosive hazard
DEVCOM	US Army Combat Capabilities Development Command
DOD	Department of Defense
EM	electromagnetic
GPR	ground penetrating radar
H-H	horizontal-horizontal
HPC	high-performance computing
IED	improvised explosive device
LOS	line-of-sight
PSF	point spread function
RCS	radar cross section
RMS	root mean square
Rx	receiver
SAR	synthetic aperture radar
SPM	small perturbation method
TCR	target-to-clutter ratio
Tx	transmitter
UAV	unmanned aerial vehicle
UWB	ultra-wideband
V-V	vertical-vertical

1 (PDF)	DEFENSE TECHNICAL INFORMATION CTR DTIC OCA
1 (PDF)	DEVCOM ARL FCDD RLD DCI TECH LIB
5 (PDF)	DEVCOM ARL FCDD RLS ES T DOGARU C LE K SHERBONDY K GALLAGHER B PHELAN